MASTERARBEIT

Titel der Masterarbeit

Investigation of Prompt Gamma Imaging as
Range Verification Method
for Ion Therapy

verfasst von

Florian Michael Pipper, BSc

angestrebter akademischer Grad

Master of Science (MSc)

Wien, 2015

Studienkennzahl lt. Studienblatt:	A 066 876
Studienrichtung lt. Studienblatt:	Physik
Betreuer:	Dr. Johann Zmeskal, Privatdoz.

Abstract

Ion therapy has become one of the major pillars in modern cancer therapy with several dedicated therapy centres all over the world. However, there still exists no satisfying imaging technique that could be used for an online quality control. The detection of prompt gamma rays presents a promising approach. This secondary radiation is created in inelastic nuclear reactions of the primary beam on a timescale below nanoseconds. The production rate is correlated to the energy deposition and it should therefore be possible to reconstruct the ion range from the longitudinal yield distribution.

In the scope of this work I investigated several topics concerning prompt gamma imaging, making use of both simulations and experiment. A number of factors regarding the production and the detection of prompt gammas were evaluated with the Geant4 based toolkit GATE. A variable spectroscopy setup based on a HPGe detector was build and tested within a short beam time at the Paul Scherrer Institute in Switzerland. Based on the experience gained from those experiments, improvements of the setup were proposed and implemented.

Zusammenfassung

Ionentherapie ist zu einer wichtigen Säule der modernen Krebstherapie geworden und ist inzwischen in mehreren Therapiezentren weltweit verfügbar. Es gibt jedoch immer noch keine zufriedenstellende Möglichkeit, die durch die Ionen deponierte Dosis im Patienten nachzuvollziehen. Ein vielversprechender Ansatz ist die Detektion von prompter Gammastrahlung. Hierbei handelt es sich um sekundäre Strahlung, die in Kernreaktionen zwischen den Ionen und dem Absorbermaterial entsteht. Die Lebenszeiten der beteiligten Zustände sind dabei unter einer Nanosekunde. Die Produktionsrate dieser Strahlung ist mit dem Energieverlust korreliert und es sollte daher möglich sein, aus der longitudinalen Intensitätsverteilung auf die Reichweite der primären Ionen im Absorber zu schließen.

In Zuge dieser Arbeit habe ich mich mit mehreren Aspekten zum Thema 'Prompt Gamma Imaging' beschäftigt. Einige wichtige Eigenschaften bezüglich der Produktion und Detektion von prompter Gammastrahlung wurden durch Simulationen im auf Geant4 basierenden Toolkit GATE untersucht. Um diese Simulationen zu verifizieren, wurde ein variabler Spektroskopieaufbau basierend auf einem HPGe Detektor gebaut. Dieser wurde charakterisiert und in einer kurzen Strahlzeit am Paul Scherrer Institut (Schweiz) getestet. Beruhend auf den Resultaten dieser Strahlzeit wurden einige Verbesserungsmöglichkeiten des Aufbaus erkannt und die ersten Schritte zu deren Implementierung eingeleitet.

Acknowledgements

First and foremost, I would like to thank my supervisor Hannes Zmeskal. His support during the many months of this thesis was exceptional and he always had an open ear for my questions. I also wish to thank him for the opportunity to participate in a beamtime of an international collaboration that allowed me an inside into the workings of a group of world class scientists. On this, I would also like to thank Eberhard Widmann for the financial support and his help whenever I needed it. Leo and Mark I would like to thank for their help in preparing the beamtime and for showing me, how helpless one really is without the aid of technicians!

Next I would like to thank Julia for her everlasting patience, Hans for introducing me to the topic of my thesis in the first place, Ken for all the questions he answered, Herbert and Doris for their help and all the people from SMI for their support and the fun times we had.

Last but not least, my gratitude is to my family who is always supporting me in everything I do and also enabled me to finish my studies without the need for a side-job.

Contents

Chapter 1

Introduction

Ion therapy has become a major pillar in modern cancer treatment strategies. It presents the possibility to deliver a precisely shaped dose distribution to the tumour volume while sparing the surrounding tissue to a large extent. Though already proposed in 1946 by Robert Wilson [1], it is only in the past two decades that ion therapy has been accessible on a larger scale − mainly due to the lack of necessary infrastructure that is needed to access ions of appropriate energies. Today, there exist a number of dedicated facilities all over Europe that provide this infrastructure.

The most modern of these facilities make use of a technique called *active beam scanning* or *voxel scanning*. Here, the tumour is divided into hundreds to thousands of sub volumes called voxels, each of which is given a precise dose value by the treatment planning and irradiated independently. However, this high accuracy dose delivering is only possible if there exists an equally precise knowledge of the tumour volume and its surroundings. This is usually only the case for a very short period of time, e.g. shortly after a CT. Therefore, it is desirable to have the possibility to verify the actual delivered dose by independent means and, if necessary, adapt the treatment planning. One approach for such a verification is to infer the delivered dose distribution from the distribution of secondary prompt gamma radiation that is created during the therapy. This approach called, *prompt gamma imaging* or PGI, is the main topic of this thesis.

1.1 A Short Overview on Ion Therapy

Unlike electromagnetic radiation, the energy deposition of heavy[1] charged particles is characterised by an increase in depth, eventually ceasing in a sharp maximum close to the finite and energy dependent range. This maximum is named Bragg peak after its discoverer William Bragg. Additionally, some ion species show an elevated biological effect in this area, i.e. the same dose results in a lower cell survival rate.[2]

[1]The term 'heavy' in a medical physics context refers to any masses equal or higher than the proton mass.

[2]The quantity to describe this effect is called relative biological effectiveness and is closely related to the energy loss per distance of the ion species, the ionisation energy of the DNA molecules and the DNA repair mechanism. See Schardt et al. [2, chapter 3] for more information.

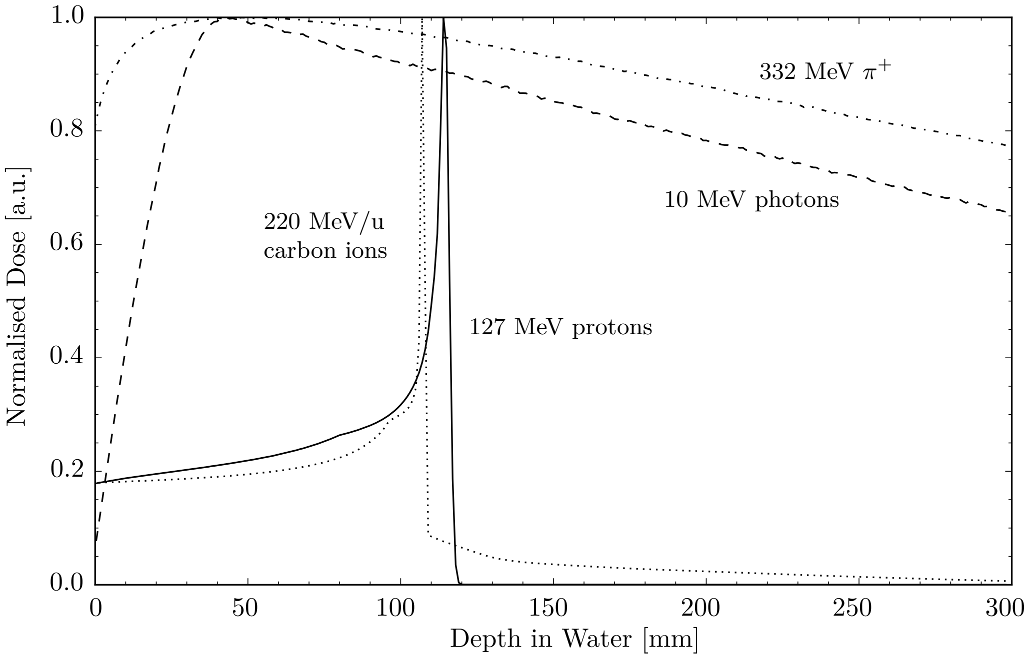

Figure 1.1: Longitudinal dose profile in water for various primary beams, normalised to the respective maximum. Protons and carbon ions show an increasing dose deposition in depth with the Bragg peak close to the end of their finite range. Notice the distal tail in the dose distribution and the much narrower Bragg peak for carbon ions compared to the profile of protons. Simulations were done with GATE.

A comparison of the depth dose profiles of several different radiation types can be seen in fig. 1.1. While photons show a maximum near the beginning followed by a slow decay, the characteristic Bragg peak is visible for all charged particles except for electrons. Due to their relatively small mass their energy loss shows a different behaviour than that of heavier charged particles. Two important differences can be seen when comparing the dose profile from protons to that of carbon ions (or any other ions heavier than protons for that matter). First, the Bragg peak of carbon ions is narrower due to their higher mass. Secondly, there is a tail after the Bragg peak in the dose distribution of carbon ions that is the result of fragmentation processes. These two characteristics will be discussed in more detail in chapter 2.

Modern ion therapy is almost exclusively based on protons and carbon ions. The use of other ion species such as helium, oxygen or neon has been investigated in the 70s [3] and is being reinvestigated in modern therapy environments [4]. Also, the potential use of anti protons is a topic of ongoing research [5]. Properties of interest for those particles include mainly biological and technical aspects. Pions are not actively used in radiotherapy applications today. Nonetheless their depth dose profile is shown in fig. 1.1, because they played an important role in the experiments that were conducted within this thesis.

Taking advantage of the energy loss characteristics of heavy charged particles, a depth dose distribution can be tailored to a target volume via superposition of different primary energies. However, as stated at the beginning, one needs exact knowledge of the tissue composition to fully exploit this potential. There are several factors that will blur that knowledge. The most important one is time.[3] The patient's internal geometry will change over the course of a treatment (which can take up to several weeks), e.g. by changes in the tissue composition or filling of cavities with fluids (see Paganetti et al. [6]). The result of these uncertainties is that the targeted volume is usually calculated with safety margins to either ensure tumour coverage or avoid damage to risky organs like the spine. Consequently, it is desired to verify the actual beam delivery within the patient to avoid the safety margins and have some sort of quality control. Ideally, this verification should be online (i.e. during the irradiation), non invasive and allow for a real time adaptation of the treatment to any changes.

1.2 Imaging Techniques for Ion Therapy

In order to monitor the actually delivered dose distribution and confirm treatment planning, many different approaches have been proposed. Probably the most apparent method is to measure the dose before it enters the patient, e.g. by an energy loss measurement in a gaseous ionisation chamber. However, such a method can only deliver information about the total dose that is delivered, not about the actual distribution and will thus not be discussed any further.

Another possibility would be to measure secondary radiation that escapes the target and to try to find some correlation with the dose deposition. Basically, this secondary radiation consists of photons, neutrons and protons (and other light ions) and, as a special case, photons having 511 keV from beta plus emitters. The three former types of radiation are called *prompt* because they are created in nuclear reactions on a sub nanosecond timescale while the latter is called *delayed* due to the lifetime of the beta plus emitters that is on a timescale of seconds to minutes for the emitters of interest. Also, Cherenkov radiation from secondary electrons can escape the body under certain circumstances and lately there have been approaches to measure ultrasound signals created by thermoelastic expansion of tissue. Except for neutrons, each of the secondary radiation types has been proposed to offer information about the dose distribution. The following section should provide a short overview on the different imaging approaches for ion therapy and their current research status.

1.2.1 Positron Emission Tomography

The only clinically used online technique for imaging of the dose distribution in ion therapy today, is *Positron Emission Tomography* or PET. Nuclear spallation reactions of target and, in the case of carbon irradiation, also projectile nuclei, can create beta plus emitters. Some of them have well suited half lifes for a PET scan during or shortly after the irradiation, e.g. ^{10}C (19.3 sec), ^{11}C (20.3 min) or ^{15}O (122.2 sec). The two resulting 511 keV photons are emitted in a nearly 180 degree angle[4], which, if detected in coincidence, can

[3]There are other uncertainties like patient movement and inaccurate positioning. However, these factors are easier tackled with other approaches such as laser tracking.

[4]The actual angle varies slightly from 180 degrees due to momentum conservation. This ultimately limits the achievable spatial resolution with PET. However, at the moment other factors present much stricter limits.

be assigned to a so called line of response that contains the point of origin. Like for many other imaging techniques, the distribution of the activated emitters is different from the dose distribution with a drop in activation a few millimetres before the dose falloff [7]. The obtained PET image is compared to expectations from the treatment planning, i.e. Monte Carlo simulations.

If the PET scan is carried out after the irradiation, one speaks of offline PET. This option has the advantage, that conventional scanners can be used and no technical adaptations are needed. However, offline PET scanners will be situated outside of the treatment room and thus require a relocation of the patient. The time needed for the relocation (seldom faster than 15 minutes [8]) leads to a biological washout of the long-lived emitters and practically a complete loss of the short-lived once. The latter is of even more significance for proton therapy in which projectile fragmentation is missing and ^{15}O with roughly 2 minutes half life is the emitter most created.

To avoid the inevitable washout and statistics loss in offline PET, in-beam or online PET is used. Here, the scanner is incorporated into the treatment room and measurement is conducted during or immediately after the therapy session. While solving the afore mentioned problems, the limited place available inside a treatment room poses a new obstacle. At GSI, a double headed BGO positron camera was used to avoid interference with the beam line and positioning system [9]. This not only drastically reduces statistics compared to a full ring scanner but also leads to artefacts in the image reconstruction. Another problem is the high rate of prompt gamma radiation causing false coincidences. Therefore, it is envisaged to record data only if the beam is off, e.g. during the injection phase in modern facilities.

An overview of several years of offline PET experience at MGH Boston and online PET usage at GSI can be found in Parodi et al. [8].

1.2.2 Interaction Vertex Imaging

Interaction Vertex Imaging or IVI uses prompt charged particles produced over a wide angular and momentum range to reconstruct nuclear emission vertices. Since secondary fragments have about the same velocity as primary particles but lower charge states and masses (see chapter 2), their range is generally longer and thus mostly highly energetic prompt protons emerge from the target. The main idea is to measure the direction of these forward ejected protons by two consecutive tracking detectors and combine this information with a beam hodoscope to reconstruct a map of the interaction vertex density inside the target. This density map should then provide information on the dose distribution. Difficulties include the multiple scattering of protons inside the target, large influences of the target's geometry and the unclear correlation between Bragg peak and vertex density.

Henriquet et al. conducted a first measurement of secondary proton yields together with extensive simulation studies [10]. They used a set-up of a single tracking detector and a beam hodoscope and report that roughly half of the protons are emitted at angles smaller than 40 degrees. This is valuable information since the angle of the tracking detectors with respect to the beam axis is a trade off between statistics and precision. Their simulation results also show that the blurring from vertices produced by secondaries will not be too problematic due to the low energies of the emitted protons from these points.

In 2013, Gwosch et al. reported first reconstructions with a setup of two silicon pixel detectors situated at 30 degrees 1 metre upstream of the target and no hodoscope. They used a back projection method and tried different fitting approaches to correlate one fitting parameter to the primary beam range, the beam width and the beam position. While giving sub millimetre precision for the beam width and beam position measurement, the precision for the beam range varies between 1.3 and 2.8 millimetres depending on the fitting approach [11]. They suggest that a set of multiple detectors at different positions should provide a stable empirical relationship between ion range and vertex distribution. This would also allow for more advanced reconstruction algorithms. It remains to be seen if differences in geometry will allow for the same empirical correlation or if one can find suitable models that provide a more stable reconstruction. Also, it is questionable to what extent this technique will be suitable for proton therapy due to the much lower yields of highly energetic prompt protons.

1.2.3 Ionoacoustic Imaging

Very recently another approach has been presented that takes advantage of the induced temperature raise caused by ion irradiation. These variations are in the order of millikelvins and microseconds. The following thermoelastic expansion of the tissue produces acoustic waves on an ultrasonic scale that can be recorded by common ultrasonic sensors. The distance between target surface and Bragg peak can be deduced from the time difference of the sound waves arriving at the sensor.

Assmann et al. reported a first Bragg peak determination for 20 MeV protons in water using a commercially available piezo-composite (PZT) based ultrasound immersion transducer that can be used at 3.5 or 10 MHz. The detector was positioned at the distal end of the water target on the beam axis. They measured a mean value of 4239±30 µm and 4255±30 µm at 3.5 and 10 MHz respectively, compared to a Geant4 result of 4060 µm [12]. As explanation of this discrepancy, they point out various dependencies that are not yet fully understood and require further studies, e.g. dependencies on the proton pulse width.

In conclusion, the ionoacoustic approach is still at a very early stage but can take advantage of the large amount of experience already existing in other fields of acoustics. A dedicated apparatus for ion therapy application will surely be cheaper to manufacture than for the nuclear approaches since industrial solutions for many other applications already exist. However, at the moment this approach seems to be very dependent on short and high intensity pulses and it remains to be seen how well it will stand at continuous beam extraction (lower beam intensity, no time profile) and higher proton energies. Also, in a non homogeneous target such as a real patient, there will be many surface transitions and variations in the speed of sound (body temperature, tissue density) that will have to be included in the analysis.

1.2.4 Prompt Gamma Imaging

The use of prompt gamma radiation as imaging technique for ion therapy was first proposed by Stichelbaut and Jongen [13], but prompt gamma rays from proton activation have been studied much earlier in astronomy [e.g. 14]. They result mainly from direct excitation of target nuclei or from target or projectile nuclei that are left in an excited state after nuclear spallation reactions.[5] Since their production is also caused by energy loss, they should show some correlation to the dose deposition. While this is also the case for other types of secondary radiation, the weakly interacting nature of photons in the MeV range will result in much less scattering while traversing body tissue and should therefore allow an easier reconstruction of the original production profile.

The first measurements of prompt gamma radiation from proton irradiation in a clinical environment came from Min et al. in 2006 [15]. They compared the total counts of a slit collimated (2 mm hole, well shielded) CsI(Tl) detector with the dose measurements from an ionisation chamber prior to the target and found that for primary proton energies of 100, 150 and 200 MeV the respective peaks correlate within 1 to 2 mm. Best results were reported with a lower threshold at 4 MeV.

In 2009, Testa et al. reported first results from prompt gamma measurements during carbon ion irradiation [16]. Here, the additional fragmentation processes result in much higher neutron yields. To distinguish between gamma and neutron events, they used a time of flight selection triggered by the RF-signal from the cyclotron. For the final analysis, only detector events within a 6 ns time window and above 1 MeV were selected. No reconstruction was made, but the longitudinal distribution of the selected events indicate a clear correlation to the ion range. They conclude that improving the signal-to-background ratio, whether by means of TOF or another method, is going to be a crucial aspect for this application.

Since then, several other groups have studied prompt gamma emission after proton or carbon irradiation with a spectroscopy scanning approach. Two more notable are Polf et al. [17], who showed that the intensity of the 6.13 MeV gamma line of ^{16}O is proportional to the oxygen concentration in the target and suggest the possibility to monitor the oxygen content of tissue over the course of multiple therapy sessions to track changes in the irradiated tissue, and Janssen et al. [18], who studied the influence of various parameter such as elemental composition, target diameter, energy cut-off and detector acceptance angle on the accuracy of the range prediction that can be achieved by PGI measurements. The latter conclude that 'the PG signal is rather robust to many parameter variations, but millimetre accurate range monitoring requires all medium and detector properties to be carefully taken into account'.

Detection Systems

In order to have a clinical viable imaging method, it is required to measure the complete prompt gamma production profile at one time. To achieve this, it is necessary to develop a detector system with either physical or electronic collimation that allows for spatial-resolved detection of many MeV photons. Here, three different approaches will be discussed.

One approach is to use a multi slit collimator followed by a detector that is segmented along the beam axis (see fig. 1.2(a)). Such a design has been used by Min et al. [19] using

[5] See chapter 2 for a more detailed discussion of prompt gamma production and further sources.

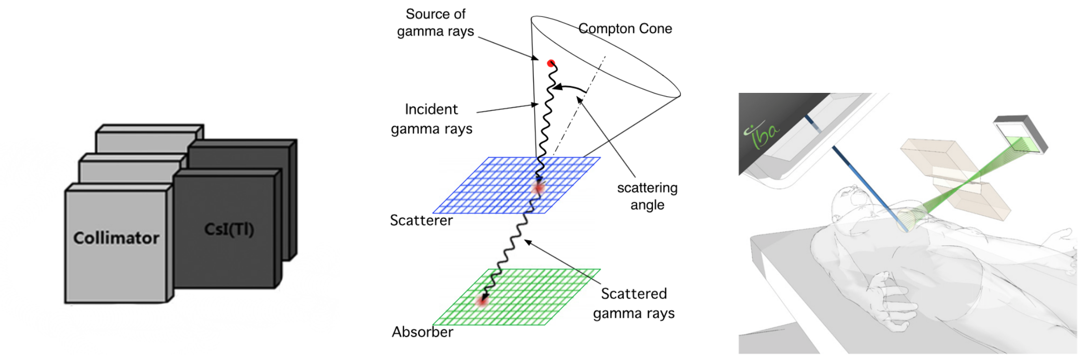

(a) multi-Slit camera (b) Compton camera (c) knife-edged slit camera

Figure 1.2: Schematics of a multi-slit camera (a, adapted from Min et al. [19]), a two stage Compton camera (b, taken from Yamaguchi et al. [20]) and a knife-edged slit camera (c, taken from Smeets et al. [21]).

a 2 mm thick collimator followed by a 2 mm gap. The collimator length was 2 mm and CsI(Tl) scintillator segments of 2 mm thickness were situated right behind the collimator gaps (a total of 35 cm from the beam axis). The measured integrated counts between 4 and 10 MeV of each segment were fitted with a sigmoidal function. They don't report a precision value but suggest that with a sophisticated analysis the Bragg peak should be detectable with an error of a few millimetre. Multiple detector elements should provide further improvement.

Another approach known from astrophysics is the Compton camera (see fig. 1.2(b)). This system consists of two consequent but separate detectors. One is optimised to detect Compton scattering and the other for photo absorption. The idea is to reconstruct the angle of the incoming photon from the two energy depositions E_1 and E_2 by

$$\cos\theta = 1 - m_e c^2 \Big(\frac{1}{E_2} - \frac{1}{E_1 + E_2}\Big) \tag{1.1}$$

If the two detectors are then segmented in three or, if thin enough, two dimensions, one can obtain the origin of the photon by intersection with the known beam axis. The big advantage of this approach is that there is no need for mechanical collimation (which is usually very bulky and heavy). However, the precision of the calculated angle heavily depends on the energy and spatial resolution of both detectors. Ideally, a good time resolution would also be desirable. Fulfilling all those requirements and at the same time retaining a high efficiency is a difficult task that many research groups are working on (though not solely for PGI). The approaches range from stacks of silicon strip detectors followed by a segmented block of CdZnTe to a gaseous TPC surrounded by a liquid scintillator. The application of PGI poses two additional problems: Unlike in astrophysics, one has to deal with limited statistics and an unknown incoming energy which imposes a difficult challenge to the image reconstruction (using only discrete lines would further decrease statistics). Variations of the two stage Compton camera are the three stage Compton camera that needs two consecutive Compton scatterings followed by a third interaction of any kind, and the pair creation camera, that tracks pair creation in e.g. a TPC and reconstructs the initial photon direction from the energy and direction of the electron-positron pair.

A third approach is the so called knife-edged slit camera, which uses a slit collimator with openings sharpened like the cutting edge of a knife followed by a segmented detector along the beam axis (fig. 1.2(c)). The idea is that in the case of a perfect collimator, any segment of the detector can only see gammas coming from a certain point along the beam axis and one would thus obtain a projection of the gamma production along this axis. Smeets et al. [21] made extensive tests with such a design. They evaluated the collimator slit angle, slit opening, material and thickness as well as detector segmentation width and thickness. As a result from optimised simulations they report range estimation of $\sigma = 1.5$ mm with 10^8 protons at 160 MeV into an PMMA target and the collimator situated 15 cm from the beam axis. An experimental validation could not completely follow up on those results but reached the same precision at about $3{\cdot}10^8$ protons. Also, this result relies on simulation to obtain reference data and was obtained at low beam currents, thus eliminating the problem of high count rates and dead time. Nonetheless, the knife-edged slit camera is able to map the longitudinal distribution of prompt gamma radiation in one single measurement as required for any real application.

Chapter 2

Theoretical Background

This chapter deals with the theoretical background of the prompt gamma production and the underlying nuclear reactions. The topics are discussed as compact as possible with a reference to more comprehensive resources where necessary.

2.1 Energy Loss and Range

The energy loss of heavy charged particles in matter can be described by the specific energy loss or linear stopping power S.

$$S = -\frac{dE}{dx} \tag{2.1}$$

In the energy region relevant for ion therapy, the dominant channel for energy loss is inelastic scattering due to Coulomb interaction with target electrons. At projectile velocities larger than a few Bohr velocities v_0 (the velocity of an electron bound by 13.6 eV) this is well described by the so called Bethe-Bloch formula. In SI units[1] it reads

$$S = -\frac{dE}{dx} = \frac{4\pi Z_p^2}{m_e v_p^2}\Big(\frac{e^2}{4\pi\epsilon_0}\Big) N Z_t \Big[\ln\frac{2m_e v_p^2}{I} + \ln\frac{1}{1-\frac{v_p^2}{c^2}} - \frac{v_p^2}{c^2} - \frac{C}{Z_t} - \frac{\delta}{2}\Big] \tag{2.2}$$

where Z_p and v_p are the charge and velocity of the projectile, Z_t and N are the atomic number and atomic density of the target, m_e and e are the mass and charge of the electron and I is the mean excitation and ionisation potential of the target.[2] The C term represents corrections due to the different binding energies of target electrons ('shell correction') and the δ term corrections due to shielding effects ('density correction'). For a detailed discussion of those terms see [22].

There are many details about this formula that deserve close attention but for the purpose of this thesis only a few points shall be discussed. First, for medium velocities, the

[1] It should be noted that the Bethe-Bloch formula is often displayed in varying arrangements and units of measurements as well as additional correction terms that are not included in here.

[2] The mean excitation and ionisation potential is the effective quantity that portraits the minimal energy loss of the projectile in one interaction with the target. Values for liquid water range from 75 eV to 80 eV [2].

Table 2.1: Penetration depth of protons in liquid water at various energies. CSDA range data taken from the NIST database [24]. Penetration depths are calculated with a density of $\rho = 0.99780$ g/cm^3 (22° C).

Kinetic Energy [MeV]	CSDA Range [g/cm^2]	Penetration Depth [cm]
50	2.23	2.22
75	4.62	4.61
100	7.72	7.70
125	11.46	11.43
127	11.78	11.75
150	15.77	15.74
175	20.62	20.57
200	25.96	25.90
225	31.74	31.67
250	37.94	37.86

energy loss rises approximately with $1/v_p^2$ and results in the advantageous profile that ion therapy is based on. At velocities much lower than v_0 the energy loss scales with v_p. The intersection of these two regions results in the Bragg peak. However, this behaviour is best modelled with a different approach than the Bethe-Bloch formalism [23]. Second, the maximum energy transfer from the projectile to one electron is approximately $2m_e v_p^2$ (constraint by kinematics) and thus secondary electrons are spatially confined close to the primary tracks. Finally, it is important to understand that the Bethe-Bloch formalism does only deal with inelastic electronic interactions and does not account for interactions with the target nuclei (elastic, inelastic or Bremsstrahlung). This is not a concern for dose calculations because the dominating mechanism of energy loss, and thus dose deposition, are the interactions with the target electron and semi-empirical corrections can be done to include the dose deposition by other mechanisms to a satisfying degree. However, it also means that the Bethe-Bloch formalism can not provide any insights into the production of secondary radiation and its correlation to the dose deposition.

From the specific energy loss one can calculate the CSDA (continuous slowing down approximation) range R.

$$R(E) = \int_0^E \left(\frac{dE}{dx}\right)^{-1} dE \tag{2.3}$$

The ranges of protons and carbon ions in water for various energies are tabulated in tab. 2.1 and 2.2.

An important aspect of the energy loss is its statistical nature. Therefore, a beam of initially mono-energetic heavy ions will always show a spread in energies after travelling through an absorber. This phenomena is called energy straggling and results in a variance σ_E^2 of the energy loss. The consequential effect is that the range of the ion is only a mean value and shows a variance σ_R^2 as well. The ratio of range straggling to mean range is proportional to the inverse square root of the projectile's mass [2].

$$\frac{\sigma_R}{R} \propto \frac{1}{\sqrt{m_p}} \tag{2.4}$$

This explains the narrower Bragg peak of carbon ions compared to protons.

Table 2.2: Penetration depth of $^{12}C^{6+}$ in liquid water at various energies. Ion ranges taken from simulation.

Kinetic Energy [MeV/u]	Penetration Depth [cm]
160	5.9
240	11.75
300	15.6
400	24.7

A more detailed analysis of the energy loss and range straggling of heavy charged particles can be found in Schardt et al. [2]. For a theoretical analysis, the paper of Fano should be considered [22].

2.2 Nuclear Reactions

While interactions with electrons govern the energy loss, interactions with the target's nuclei have influence on the dose deposition as well. First, elastic interactions with the nuclei lead to deflections of the projectile and thus cause range shifts and a broadening of the beam. Second, inelastic interactions can lead to a fragmentation of the projectile and target nucleus, resulting in multiple fragments with different ranges and, if those fragments are unstable, in additional radiation sources.

An established description for such spallation reactions is the so called abrasion-ablation model [25]. Here, it is assumed that the collision happens on a very short time scale so that the dynamics of the nucleus can be neglected and the problem reduces to high energy scattering of free nucleons (dynamical effects can be reintroduced by corrections). The reaction is then split into two parts: the abrasion step, in which the collision takes place and the nuclei are split into fragments, and the ablation step, in which the fragments 'deexcite by evaporation of nucleons or clusters' [2] until they do not have enough energy left to separate another nucleus. The remaining energy is lost via gamma radiation and represents one part of the prompt gamma radiation of interest. The other part is created by direct excitation of target nuclei [26]. A consequence of those two different production mechanisms is that one can see gamma lines from elements that are not originally contained in the experimental setup, e.g. carbon lines in water from $^{16}O(p,p'\alpha)^{12}C^{*}$.[3]

Due to the kinematics of the reaction, the secondary particles from projectile fragmentation have velocities close to that of the primary particle [2]. As a consequent, this secondary projectiles with lower mass have a longer range than the primary ones and lead to the tail in the dose profile of carbon ions. Measurements show that at a range of 16 cm only 52% of primary carbon ion reach the end of their track without fragmentation [2]. Fragmentation also leads to additional broadening of the beam and a reduction in the peak-to-entrance dose ratio.

[3] There are also gamma rays produced during nucleon-nucleon bremsstrahlung or via giant resonances [27]. However, the contributions in the energy range of interest will be negligible.

Again, the paper of Schardt et al. [2] can be named as a resource for more detailed information. For a theoretical analysis of prompt gamma production in nuclear reactions the work of Ramaty, Kozlovsky and Lingenfelter [26] should be mentioned, even though it is written with regards to astrophysics.

To summarise, the dose deposition is done mainly via inelastic reactions with electrons while the production of secondary radiation results from inelastic reactions with the nuclei. It is reasonable to assume a correlation between both mechanism but the theoretical framework for that correlation has yet to be found.

Chapter 3

Simulations

This chapter describes several Monte Carlo simulations of prompt gamma production and detection. They were of great assistance for the proper preparation of the experiments and interpretation of the data.

3.1 The Simulation Environment

All of the simulations in this chapter were implemented within the Geant4 based toolkit GATE [28]. GATE (Geant4 Application for Emission Tomography) is a scripted simulation toolkit with the purpose to adapt the sophisticated and well validated Geant4 libraries to the field of nuclear medicine. Like Geant4, GATE simulates the passage of particles through matter. While mainly created to simulate experimental setups for PET and SPECT (Single Photon Emission Computed Tomography), it currently also supports radiotherapy applications. A simple example of a GATE script can be found in appendix A.

In GATE, there are two concepts to collect information about a simulation: the Geant4 known sensitive detector volumes and the so-called actors. Both tools have to be attached to a specific volume. Sensitive detector volumes document information about individual hits like change in energy or time of interaction. One can then add so-called digitiser modules to simulate a detector readout chain. For example, the adder module combines all hits of the same track in the same volume into one single pulse. Actors are macro tools that allow to interact with the simulation in a particular manner to extract information that would otherwise be buried deep inside the Geant4 mechanics. For example, the statistics actor returns a summary of the run statistics (starting time, number of steps, elapsed real time, etc.) and the production and stopping actor counts the number of particles produced/stopped inside a given volume. It is also possible to provide actors with a filter to, say, only record the production of photons created in a 10 degree cone around the y axis. The working principle of the different actors and digitisers will be explained later in the text when those actors are used for the first time. More information on actors, sensitive detectors and GATE in general can be found on the OpenGATE collaboration wiki [29].

All simulations have been carried out in GATE v6.2 (based on Geant4 v9.5 p01) and, if not specified otherwise, use 10^7 primary protons and 10^6 primary carbon ions.[1]

3.1.1 The Physics Lists

The selection of the physics list is a delicate problem because it highly influences the outcome of a simulation. Each list consists of a different set of physical processes and for each process a computational model is selected to describe it. For electromagnetic processes such as photo-absorption or bremsstrahlung, the choice of the model is not much of a concern since those processes are well understood and models that are valid over a large range of energies are available. For nuclear processes however, the choice of the model is essential.

In Geant4 (and thus GATE), nuclear collisions are divided into four steps [27]: application of the cross sections, modelling of intra-nuclear interactions, modelling of the pre-compound stage and modelling of de-excitation processes. For medical applications up to a few hundred MeV, the QGSP_BIC_HP list is recommended which uses the Binary Cascade model (BIC) for the first two steps at particle energies below a few GeV and the G4PrecompoundModel for the latter two.[2] Additionally the High Precision Neutron Package (HP) is used for neutron transport below 20 MeV.

A short overview of the physics models in Geant4 is available at [30]. The complete reference can be found in the Geant4 Physics Reference Manual [31].

3.2 Production Studies

To study the production of prompt gammas, a Gaussian shaped proton or carbon beam with a spread of $\sigma = 3$ mm was shot into a cylindrical water target with radius $r = 10$ cm and length $l = 50$ cm. Beam and target were aligned along the z axis. Attached to this target were different actors.

3.2.1 Production Spectrum

A first test of the simulation environment was done by looking at the production spectrum created by primary carbon ions and protons inside the water target. The spectrum was recorded by attaching an *energy spectrum actor* to the target. This device records the initial kinetic energy of every particle that enters the associated volume (creation equals entering). One can think of the energy spectrum actor as a 'perfect' detector that is neither exposed to a limited energy resolution nor to a decrease in efficiency.[3]

[1] On the average, a simulations with 10^7 primary protons takes about 12 hours while a simulation with the same number of carbon ions takes about two weeks when conducted on a modern CPU (using a single core). Thus the number of primary carbon ions was reduced to allow for reasonable simulation times. In most cases, statistics should not suffer too much due to the higher secondary yields from carbon ions.

[2] QGSP stands for quark gluon string pre-compound model and is the standard model for hadronic interactions above a few GeV. Therefore, it should not have any effect on the presented simulations.

[3] For any visualisation however, the energy resolution has to be finite. For fig. 3.4(c) it was set to 1 keV.

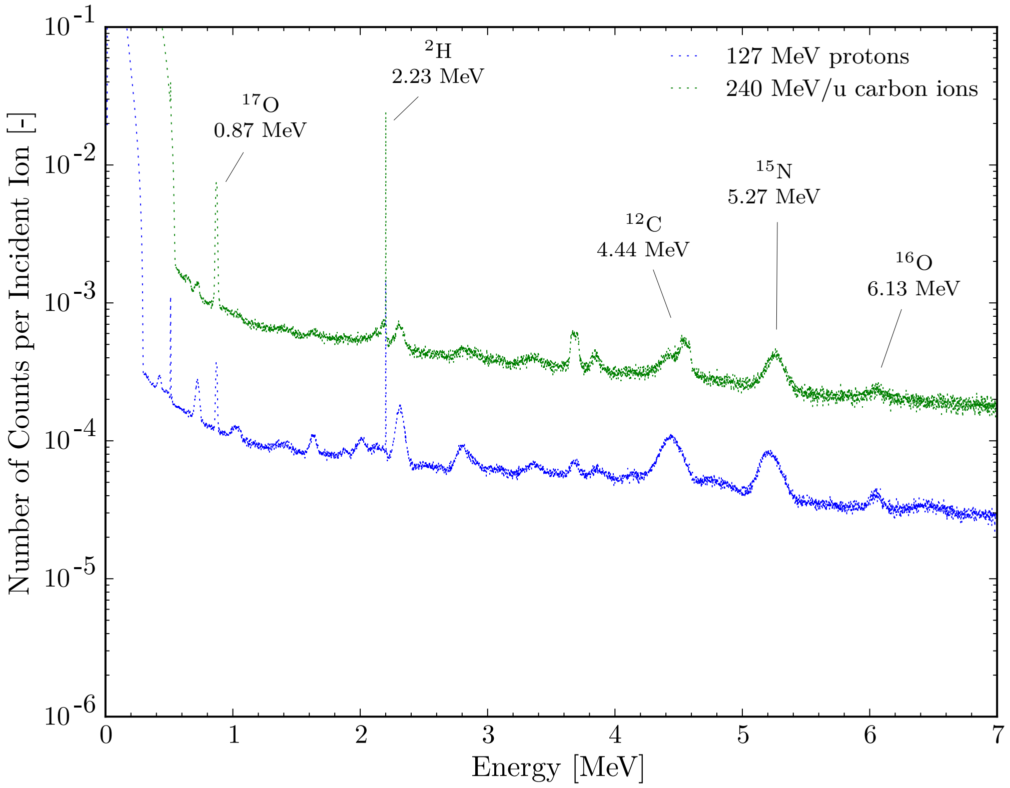

Figure 3.1: Production spectrum for 127 MeV protons and 240 MeV/u carbon ions impinging on a water target. The spectrum was recorded with an energy spectrum actor in GATE. The broad peaks are most likely the result of Doppler broadening of excitation lines due to their short lifetimes. See tab. 3.1 for a more complete list of the excitation lines.

The result from this simulation is displayed in fig. 3.1. One can see that the yields from carbon irradiation are generally higher and that some gamma peaks are more distinct in one spectrum than in the other. The latter is due to different production ratios between gammas on the one hand (discrete production spectrum) and neutrons and protons on the other (continuous production spectrum). A list of the most important gamma decay lines from relevant elements is given in tab. 3.1. It is interesting to see that for some of the excitation levels, the spectrum shows broad peaks instead of sharp lines. This is thought to be due to Doppler broadening of levels with an extremely short lifetime. For example, the prominent 4.44 MeV line of ^{12}C has a lifetime of about 42 fs. The excitation is created in a $^{16}O(p,p'\alpha)^{12}C^{*}$ reaction and will most likely decay before the recoil nucleus is at rest. In contrast to that, the 0.87 MeV line of ^{17}O has a lifetime of about 180 ps and shows a much sharper peak. The 0.511 and 2.225 MeV line, that result from positron annihilation and neutron capture respectively, show sharp peaks as well because both processes show high cross sections only when the particles are close to rest.

3.2.2 Production Rate

In order to get an estimation of the event rate, simulations of the production of secondary particles were done. The number of produced particles was recorded with a *production and*

Table 3.1: Most important excitation lines produced in water. The spectrum is shown in fig. 3.1. Data is adapted from NuDat [32].

Species	E_γ [MeV]	Lifetime [ps]	Transition
^{11}C	2.00	0.007	$\frac{1}{2}^-$ 2.00 $\rightarrow$ $\frac{3}{2}^-$ g.s.
^{12}C	4.44	0.042	2^+ 4.44 $\rightarrow$ 0^+ g.s.
^{13}C	3.68	0.001	$\frac{3}{2}^-$ 3.68 $\rightarrow$ $\frac{1}{2}^-$ g.s.
^{16}O	6.13	18.4	3^- 6.13 $\rightarrow$ 0^+ g.s.
	6.92	0.005	2^+ 6.92 $\rightarrow$ 0^+ g.s.
	7.12	0.008	1^- 7.12 $\rightarrow$ 0^+ g.s.
^{17}O	0.87	179.2	$\frac{1}{2}^+$ 0.87 $\rightarrow$ $\frac{5}{2}^+$ g.s.
	2.18	0.08	$\frac{1}{2}^-$ 3.06 $\rightarrow$ $\frac{1}{2}^+$ 0.87
^{14}N	2.31	0.068	0^+ 2.31 $\rightarrow$ 1^+ g.s.
	1.64	0.005	1^+ 3.95 $\rightarrow$ 0^+ 2.31
	4.92	0.005	0^- 4.92 $\rightarrow$ 1^+ g.s.
	2.79	4.35	2^- 5.11 $\rightarrow$ 0^+ 2.31
	5.11	4.35	2^- 5.11 $\rightarrow$ 1^+ g.s.
	3.38	0.011	1^- 5.69 $\rightarrow$ 0^+ 2.31
	5.69	0.011	1^- 5.69 $\rightarrow$ 1^+ g.s.
	0.73	8.3	3^- 5.83 $\rightarrow$ 2^- 5.11
	3.89	0.111	1^+ 6.20 $\rightarrow$ 0^+ 2.31
^{15}N	5.27	1.8	$\frac{5}{2}^+$ 5.27 $\rightarrow$ $\frac{1}{2}^-$ g.s.
	5.30	0.017	$\frac{1}{2}^+$ 5.30 $\rightarrow$ $\frac{1}{2}^-$ g.s.
	1.88	0.012	$\frac{5}{2}^+$ 7.16 $\rightarrow$ $\frac{5}{2}^+$ 5.27

stopping actor attached to the water target. This device records all produced and stopped particles inside a certain volume (or slices of that volume) and creates a map of particle production and stopping. The resolution and dimension of the map can be adjusted and was set so that the target was divided into 500 equal steps along the z axis but only one along the x and y axis. Therefore, the production was integrated over the complete radius of the volume with a 1 mm resolution along the beam axis. Several particle and energy filters were used.

Production on the Full Energy Scale

In fig. 3.2 and fig. 3.3 one can see the production of secondary particles per millimetre penetration depth. The results were obtained with a primary beam of 127 MeV protons and 240 MeV/u carbon ions respectively. These energies were chosen because their CSDA range of 117.5 mm is a typical value in clinical applications. In these two simulations, no energy cuts were set.

For the gamma production, the actual numbers close to the Bragg peak region are displayed in tab. 3.2. One can observe a drop of over 90 percent of gamma production between 109 mm and 118 mm for protons and between 114 mm and 117 mm for carbon ions. This is in concord with the dose profiles shown in fig. 1.1. Also, the narrower Bragg peak and the tail are visible in the production profile of carbon ions. At this point it is very important to note that those numbers are produced by Monte Carlo calculations and should therefore only be seen as rough estimation. Absolute numbers do not only change from simulation to simulation (as expected due to statistics) but also with the choice of the physics model. Therefore, a comparison of production and dose profile in the scope of these simulations can only be of rough qualitative nature and should not be used to interpret the relation of dose deposition and secondary gamma production.

For secondary proton production one can see a less significant drop only in the case of the primary proton beam. However, this situation changes drastically if one looks at the specific energy ranges, which will be done in the next section. For neutrons, a decrease is visible but it is neither sharp nor significant.

Noteworthy are the total production rates. For primary protons, the ratio of photons to neutrons to protons is about 1 to 0.04 to 0.3. In the case of a primary carbon beam, one observes generally higher production rates and the ratio becomes about 30 to 2 to 4. One should take remark of the much higher neutron yields from primary carbon ions which indicate that differentiation between secondary neutrons and photons is going to be of even more importance for imaging in carbon therapy.

Production in Different Energy Regions

While the study of the production in the full energy range is important to get an idea of the yields, any imaging method is primarily concerned with what can be detected rather than what is produced. For example, low energetic photons and low to medium energetic protons have too short attenuation lengths to escape the patients body and reach any kind of detector. Therefore, it is of importance to look at the different energy regions. In

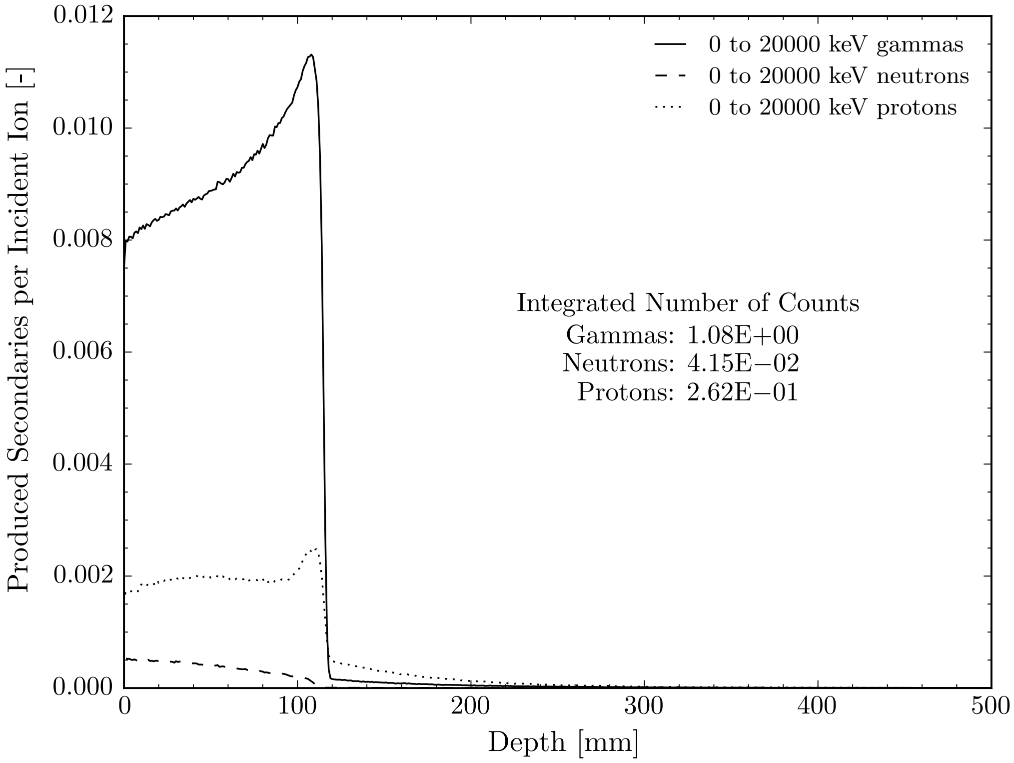

Figure 3.2: Production per mm in the energy range of 0 to 20000 keV for 127 MeV protons impinging on a water target.

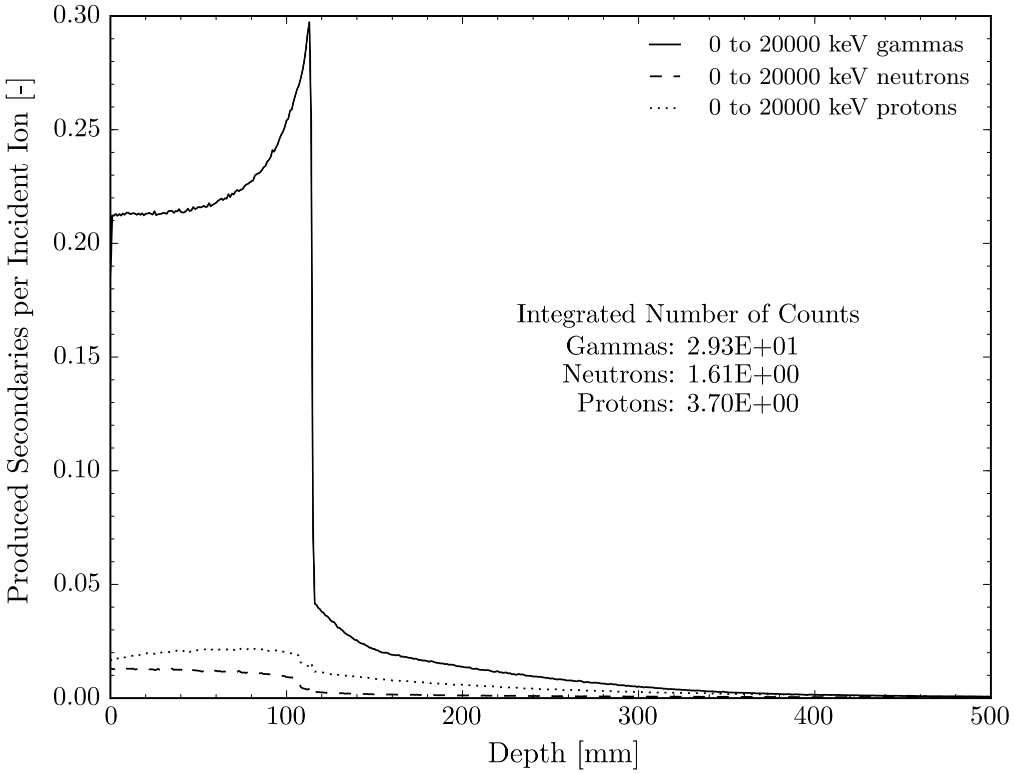

Figure 3.3: Production per mm in the energy range of 0 to 20000 keV for 240 MeV/u carbon ions impinging on a water target.

Table 3.2: Prompt gamma production along the beam axis for 127 MeV protons and 240 MeV/u carbon ions impinging on a water target. One can observe a drop of over 90 percent of gamma production between 109 mm and 118 mm for protons and between 114 mm and 117 mm for carbon ions. The values are extracted from simulations in GATE using a production and stopping actor.

Penetration Depth [mm]	Gamma Counts from 10^7 p^+	Gamma Counts from 10^6 C^{6+}
108	$1.13 \cdot 10^5$	$2.70 \cdot 10^6$
109	$1.13 \cdot 10^5$	$2.72 \cdot 10^6$
110	$1.13 \cdot 10^5$	$2.76 \cdot 10^6$
111	$1.11 \cdot 10^5$	$2.80 \cdot 10^6$
112	$1.08 \cdot 10^5$	$2.86 \cdot 10^6$
113	$1.04 \cdot 10^5$	$2.93 \cdot 10^6$
114	$0.95 \cdot 10^5$	$2.97 \cdot 10^6$
115	$0.79 \cdot 10^5$	$2.51 \cdot 10^6$
116	$0.55 \cdot 10^5$	$0.76 \cdot 10^6$
117	$0.27 \cdot 10^5$	$0.42 \cdot 10^6$
118	$0.10 \cdot 10^5$	$0.41 \cdot 10^6$
119	$0.03 \cdot 10^5$	$0.40 \cdot 10^6$
120	$0.02 \cdot 10^5$	$0.39 \cdot 10^6$

fig. 3.4 the production per millimetre from a primary proton beam is shown with various energy cuts. The choice of the cuts is based on previous simulation results but is still rather arbitrary.[4]

The drop in the gamma production is visible in all energy regions except for the very highest above 10 MeV. The region between 2.2 and 2.3 MeV is of special interest. It contains the deuterium line at 2.2248 ± 0.0010 MeV [33], produced by neutron capture on a hydrogen atom. Due to the high probability for elastic scattering of neutrons and the fact that the absorption is most probable at the end of the neutron path, it is generally assumed that this line cannot be correlated to the Bragg peak and has therefore to be excluded. However, these first simulations of the production do not suggest any of this: a clear drop in the rate is visible here as well.

For protons, there are very clear drops visible at higher energies (in contrast to the full energy range). Since protons have only a short range in tissue (about 4 mm at 20 MeV), only high energy protons can leave the patient's body during irradiation and can be detected. Thus, as discussed in the first chapter, the possibility of interaction vertex imaging appears to be another promising approach for ion range verification. The neutron production does show a slight drop in the higher energy regions, but due to the difficulties of detecting neutrons efficiently with a decent energy resolution and the already mentioned problem of elastic scattering, they will not be further analysed here.

In fig. 3.5 the same plot series is shown for a primary carbon beam. Besides minor differences in the overall shape and the already mentioned increase of neutron production, one can see that there is a higher tendency to produce high energetic photons than for primary protons. Also, when looking at the photon production between 2.2 to 2.3 MeV,

[4] For the image reconstruction, it might be more important to study the different energy regions and distinguish between them.

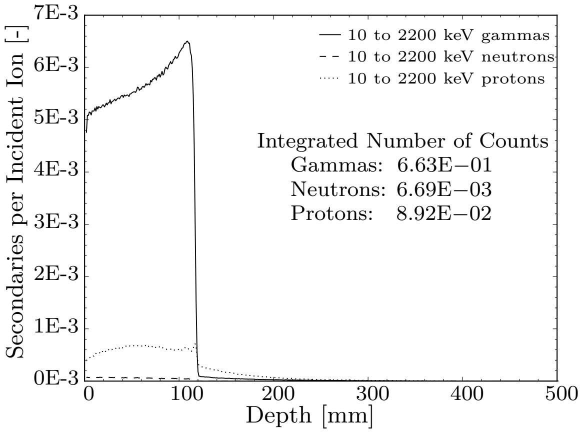

(a) 10 to 2200 keV

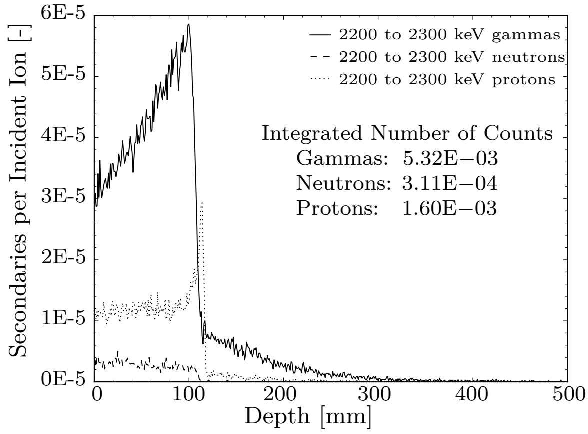

(b) 2200 to 2300 keV

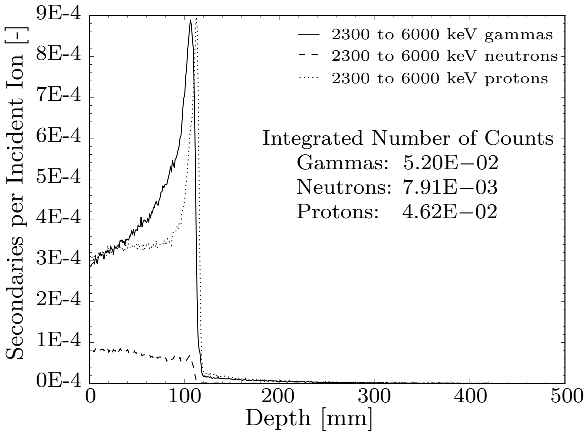

(c) 2300 to 6000 keV

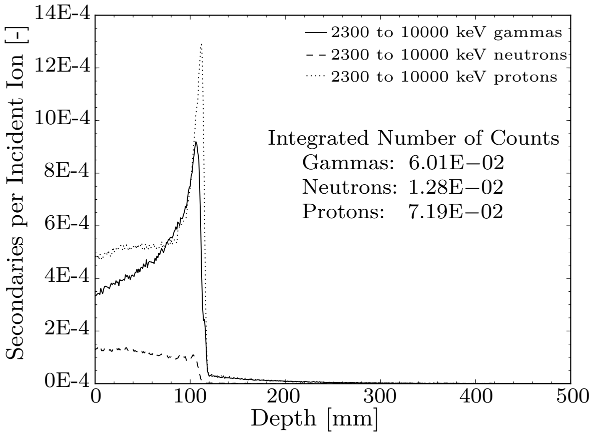

(d) 2300 to 10000 keV

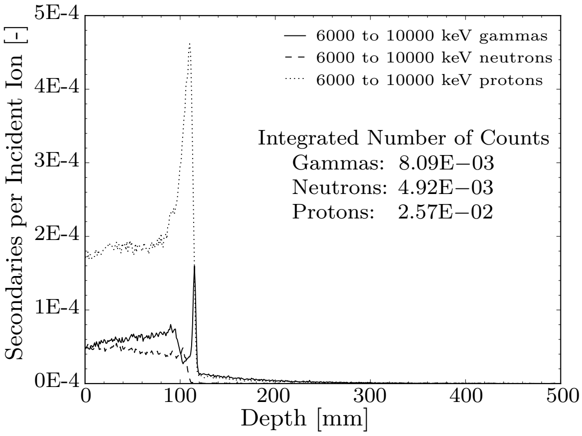

(e) 6000 to 10000 keV

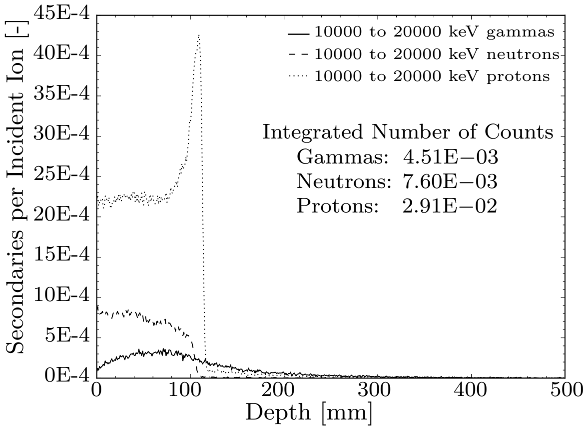

(f) 10000 to 20000 keV

Figure 3.4: Production per mm for 127 MeV protons impinging on a water target with various energy cuts between 10 and 20000 keV.

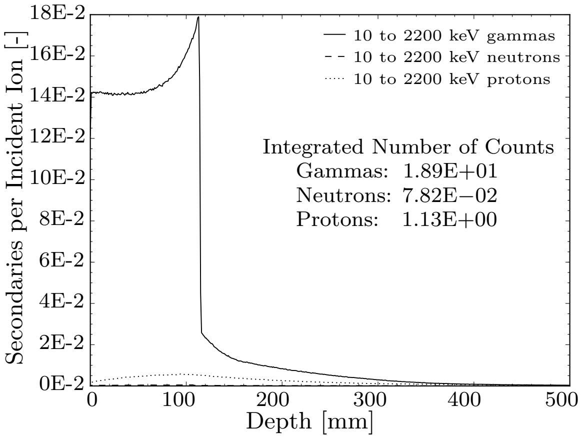

(a) 10 to 2200 keV

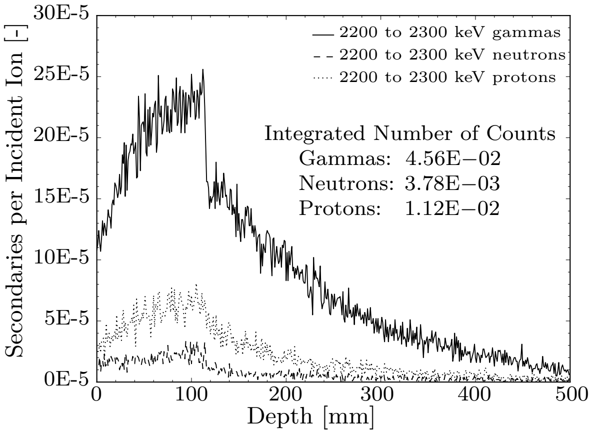

(b) 2200 to 2300 keV

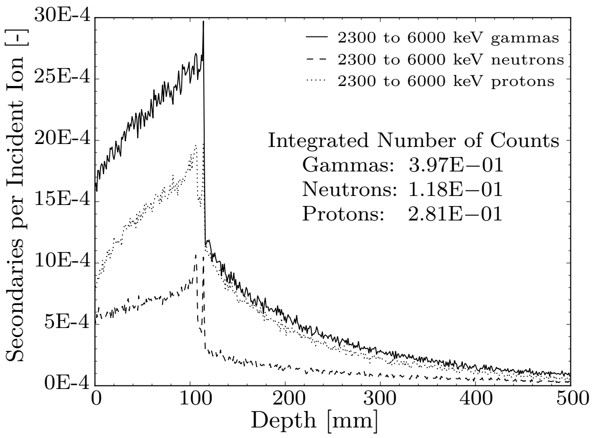

(c) 2300 to 6000 keV

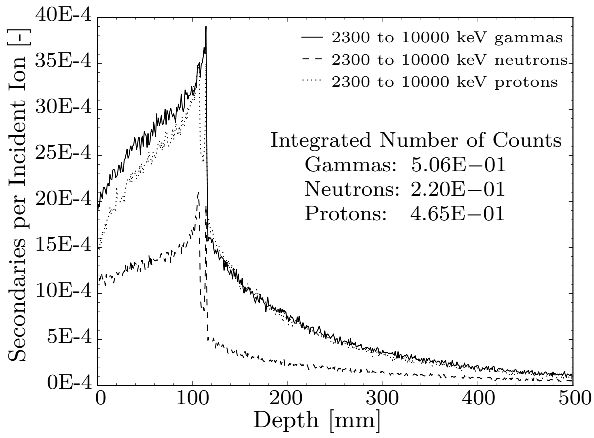

(d) 2300 to 10000 keV

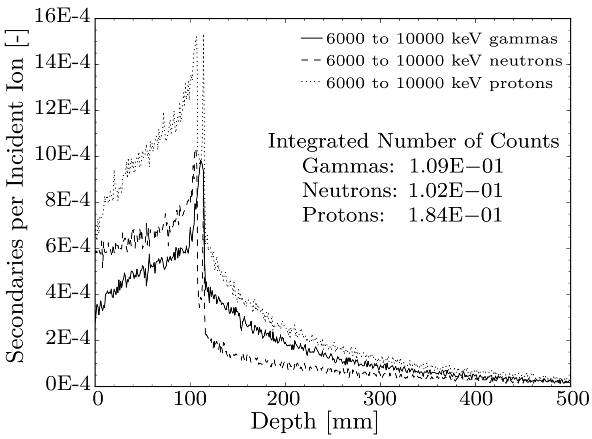

(e) 6000 to 10000 keV

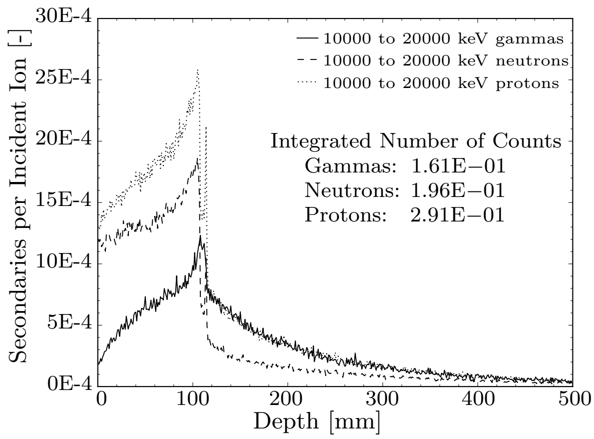

(f) 10000 to 20000 keV

Figure 3.5: Production per mm for 240 MeV/u carbon ions impinging on a water target with various energy cuts between 10 and 20000 keV.

it is more vivid now that this region should be excluded.

One more thing that sparks interest is a drop in the count rate shortly before the Bragg peak in the production of neutrons and protons above 2.3 MeV. This might be a real effect but could just as well be a wrong cross section or a bug in the simulation mechanics. In case this is a real physical effect, it might prove problematic for any imaging method detecting protons (or neutrons) and should be investigated in more detail.

When comparing the numbers from the different energy ranges, one has to keep in mind that those are Monte Carlo simulations and thus variations in the order of $\sqrt{N}$ are expected.[5]

3.2.3 Correlation Between Dose and Gamma Production

In fig. 3.6 the gamma production per millimetre is displayed together with the dose deposition for various primary proton energies. The end points of both distributions seem to coincide very well. However, one has to keep in mind, that the resolution was only set to 1 mm in a homogeneous target and that the simulation should naturally be viewed with a healthy scepticism. A high precision measurement of the production cross sections would certainly be of great interest for PGI. Verburg et al. [34] tried to collect cross section data from various resources (mainly astrophysics) to evaluate hadronic physics models but the data is incomplete.

A further analysis of the correlation between dose deposition and gamma production is outside the scope of this thesis. It would be very interesting to see how well certain points and extrapolations of both distributions coincide. On the basis of fig. 3.6, the intersection between the x axis and a linear fit along certain points on the distal fall off slope, say between 80% and 20% of the maximum, could be an interesting candidate. Also, one would have to check different energy regions, statistical variations and especially inhomogeneous targets.

In conclusion, the results from the production simulations suggest a high potential for any imaging technique that is based on spatial-resolved gamma or proton detection.

3.3 Detection Studies

For the detection studies, the original arrangement of beam and target were left unchanged but additional detector structures were added. The detector consisted of a sensitive detector volume made of germanium. This volume records information about every single interaction. To simulate a real detector, a set of digitisers were added. An *adder module* was used to combine all the energy depositions of the same particle in the same volume into one pulse. A *blurring module* was used to simulate the statistics of charge collection. The resolution was set to 0.13% at 1332.5 keV and scaled with an inverse square law, i.e. $1/\sqrt{E}$. Finally a *threshold module* at 50 keV was added to discard low energy events.

[5]Mind that N is always given per primary particle of which there are 10^7 and 10^6 respectively.

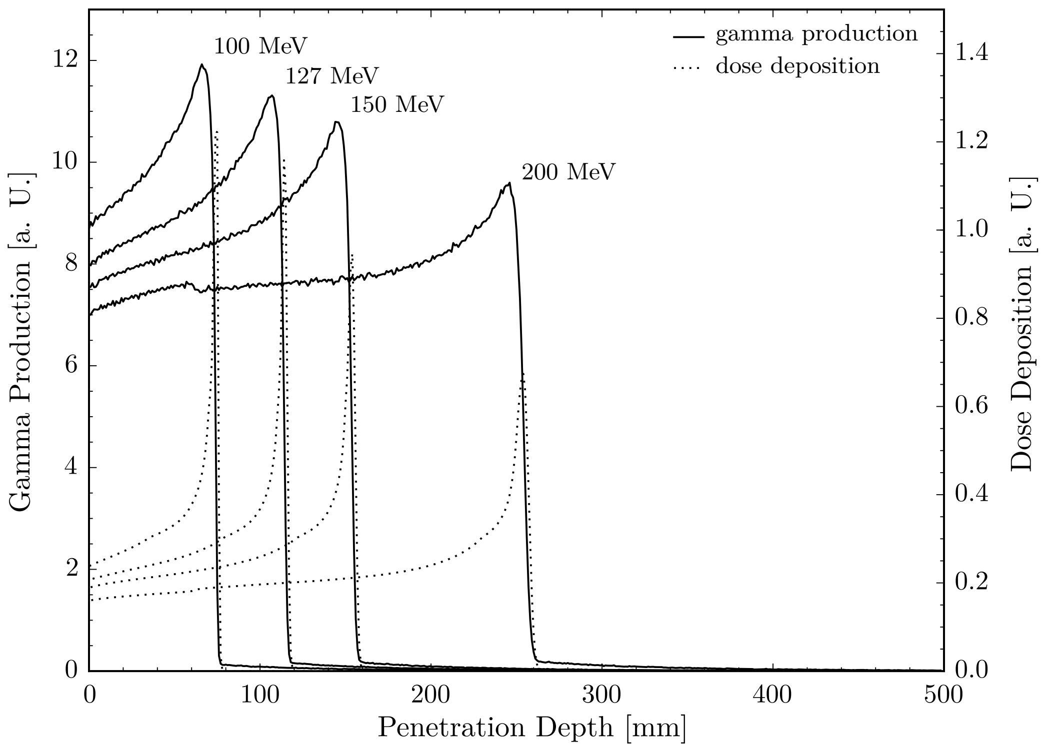

Figure 3.6: Dose deposition and gamma production per mm in the energy range of 0 to 20000 keV for 100, 127, 150 and 200 MeV protons impinging on a water target. Within a limited spatial resolution of 1 mm, the end points of both distributions coincide. Simulations were done in GATE using a dose actor and a production and stopping actor.

3.3.1 Simulated Detection Spectrum

The spectrum of particles was detected with a large barrel detector of length 70 cm centred around the target. The inner radius was 40 cm from the beam axis and the detector thickness was 10 cm. Despite this huge detector, the number of events was low and the spectrum was smoothed for display purposes using a first order Savitzky–Golay filter with a window size of 3 neighbouring data points.

The result can be seen in fig. 3.7. All lines from the production spectrum in fig. 3.1 and tab. 3.1 are visible, though some of them are not very distinctive due to the low statistics.

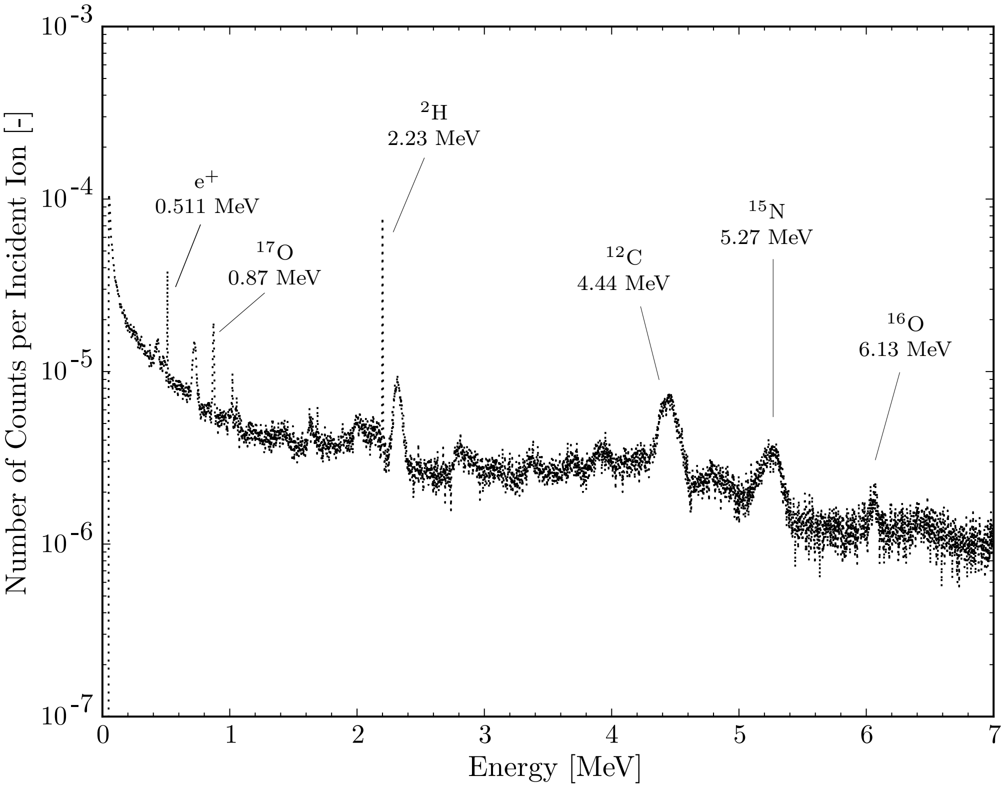

Figure 3.7: Spectrum detected by a HPGe barrel detector surrounding the water target. Due to low statistics the spectrum was smoothed using a first order Savitzky–Golay filter with a window size of 3 neighbouring data points. Incident particles are 127 MeV protons. Simulation in GATE with a sensitive detector volume attached to the germanium barrel.

Chapter 4

Experiments

The main purpose of this work was the experimental validation of the results presented in the last chapter. The original goal was to measure the longitudinal and angular distribution of the prompt gamma production using various primary energies. However, due to the limited beamtime available, only a fraction of these measurements were actually carried out within the period of this Master's thesis.

This chapter deals with the characteristics of the experimental setup, the preparations and results of the first beam time as well as the following improvements of the setup.

4.1 Experimental Setup

The setup should be versatile and allow for a free adjustment of the relative angle and position between detector and target. As projectiles, protons with energies between 100 and 200 MeV as well as carbon ions between 120 MeV/u and 400 MeV/u should be possible.

The target is a water filled plastic cylinder of 50 cm length and 10 cm radius. Water as a material was chosen due to the price and simplicity of preparation as well as the large number of available reference data and cross sections. The dimensions fit for all desired penetration depths (see tab. 2.1 and 2.2).

The detector is mounted on a rotatable platform which in turn is mounted on a sledge that is moveable in x and z direction relative to the target platform. A CAD drawing of the complete setup can be seen in fig. 4.1 and an annotated outline of the important parts in fig. 4.2.

4.1.1 Choice of the Detector

A HPGe (high purity germanium) detector was chosen to record the nuclear reaction spectrum. The cylindrical crystal has a length of 72.4 mm and a surface area 27.33 cm^2 (radius 2.95 cm).

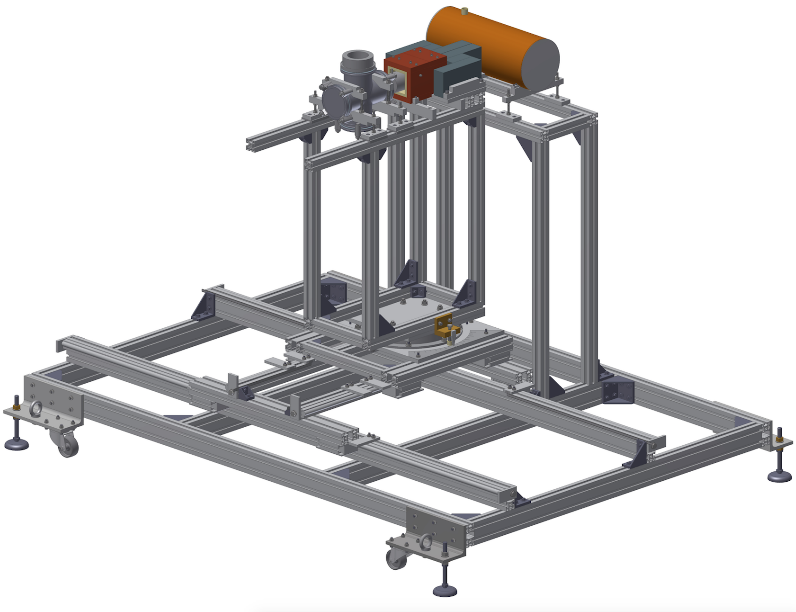

Figure 4.1: Bird's-eye view of the experimental setup. The target (orange) is mounted on a fixed platform. The detector is surrounded by a copper/plastic shielding (red) and lead collimators (dark grey). It is mounted on a rotatable disk that can be moved on a sledge along the supporting rack.

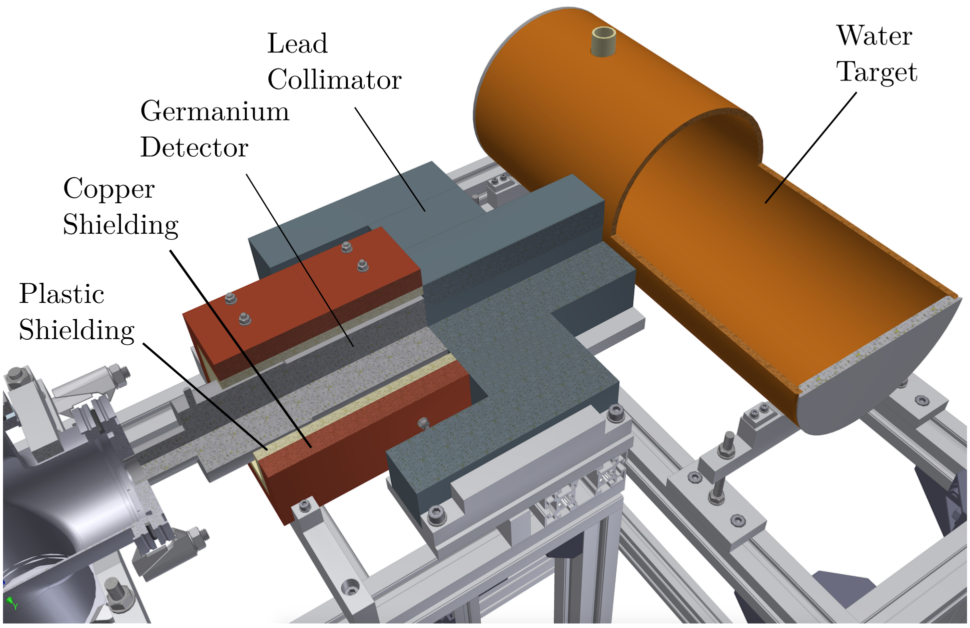

Figure 4.2: Outline of the experimental setup.

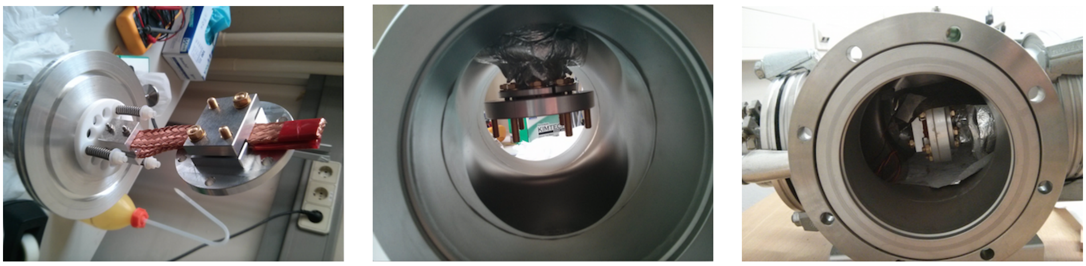

(a) detecor side (b) coldhead side (c) connection

Figure 4.3: Connection between detector and coldhead. A short copper band (a) serves as heat link between the detector and the coldhead projection (b). The connection (c) is greased with a silver containing paste.

The signal chain consisted of the pre-amplifier integrated in the detector housing, a discriminator, a standard spectroscopy amplifier (Canberra 2020) and a pocket MCA (Amptek MCA8000A). This MCA is based on a 14 bit successive approximation ADC (about 16k channels) that is read out via a programme called ADMCA (also Amptek). The analysis of the recorded spectra was mostly done either within this programme or with self-written code (NumPy or ROOT). A trigger gate was created from the original signal to reduce the effect of noise coming from the electronics.

Due to the inconvenient handling of a dewar when tilted, the detector was not cooled with liquid nitrogen but with a cryostat. For the connection between coldhead and detector, a custom made adapter was used to keep the heat link as short as possible (see fig. 4.3). The connection was then wrapped in super insulation foil (Mylar®), placed in a vacuum chamber and evacuated to 10^{-7} mbar. The temperature was measured by a PT100 sensor inside the vacuum chamber and read out by a Leakshore 335 temperature controller. The stable values were 35.6 Ω or 113 K. Due to a bad vacuum inside the detector housing it was necessary to make a connection to the vacuum chamber and pump the housing directly.[1]

4.1.2 Choice of the Shielding

The shielding consists of two parts: a low energy x-ray shielding and a high energy gamma collimator. The low energy shielding is made of 1 cm thick plastic plates followed by 2 cm of copper on the outside. They are arranged in a box structure surrounding the detector with the purpose to reduce the total rate by blocking low energetic radiation scattered by the environment or the collimator. The addition of another layer of moderation and absorber material, such as paraffin and boron, is a possible improvement at a later point. For the collimation, there are six lead bricks in front and to the side of the detector. Four of them have dimensions of 20 × 10 × 5 cm and two are 10 × 10 × 5 cm. Their purpose is to create a slit collimation to allow a spatial-resolved view on gamma radiation emerging from the target. The exact arrangement can be seen in fig. 4.2.

[1]The bad vacuum in the detector housing could have been caused by a (small) leakage or wear-out of the getter materials, which are supposed to keep the detector housing at moderately low pressure levels.

Table 4.1: Measurement of net counts in the peak area and FWHM for different bias voltages and otherwise unchanged conditions. FWHM error is taken as $\sqrt{2}$ times the channel width. The value of −2700 V was chosen due to the best FWHM value and already maximised active volume.

Voltage [V]	Peak Area Net Counts [-]	FWHM [keV]
− 2500	20469 ± 144	17.14 ± 0.34
− 2600	43554 ± 209	17.48 ± 0.34
− 2650	69355 ± 264	17.06 ± 0.34
− 2700	**106188 ± 326**	**15.23 ± 0.34**
− 2750	106194 ± 326	15.61 ± 0.34
− 2800	106322 ± 327	15.43 ± 0.34

4.2 Detector Characterisation

4.2.1 Working Point

To establish the optimal working point for the HPGe detector, a scan of the bias voltage and its effect on FWHM and peak area net counts[2] was conducted. The results of this scan can be seen in tab. 4.1.

Two effects can be observed. First, the peak area net counts increase with higher voltage until it reaches a stable value and does not change any more (within the expected error). This can be explained by the size of the depletion zone which has reached its highest possible dimension at −2700 V. At this point, the active volume (and the capacity) of the crystal is maximised and therefore the efficiency as well. The second observation is a drop in energy resolution for bias voltages below −2700 V which can be explained by incomplete charge collection. A working point of −2700 V was chosen as consequence of this measurement due to the best FWHM value and already maximised active volume.

4.2.2 Energy Resolution

In fig. 4.4 one can see a sample spectrum taken from a ^{60}Co source. Calibration with the two gamma lines at 1173.2 keV and 1332.5 keV resulted in a channel width of 0.238 keV. The FWHM and energy resolution for the 1332.5 keV peak are

$$\mathrm{FWHM}_{@1332.5\ \mathrm{keV}} = (15.23 \pm 0.34)\ \mathrm{keV}$$

$$\mathrm{R}_{@1332.5\ \mathrm{keV}} = (1.143 \pm 0.026)\ \%$$

This rather low resolution for a germanium detector can be explained by the relatively high operation temperature of 113 K. At higher temperatures thermal generation of intrinsic carriers (electrons and holes) in the crystal increases, causing significantly higher statistical fluctuations and therefore degradation of the energy resolution. For comparison, a test

[2]Net counts are the number of counts in a certain region of interest after the subtraction of an estimated baseline. This was done automatically by the ADMCA programme. The exact calculation method can found in the documentation of the programme.

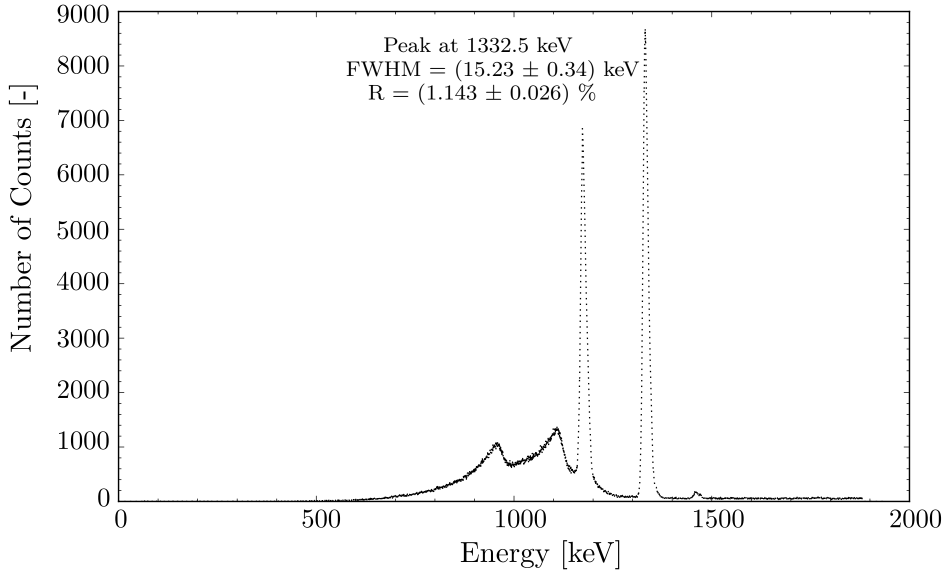

Figure 4.4: Spectrum taken from a ^{60}Co source under laboratory conditions. Peaks are at 1173.2 keV and 1332.5 keV.

measurement with a different (smaller) HPGe cooled with LN_2 to 77 K showed a resolution of (0.129 ± 0.026) % at 1332.5 keV -- an improvement of almost a factor 10.

4.2.3 Stability

In order to ensure a stable operation with cryostat cooling, a series of 21 measurements was carried out. The ^{60}Co spectrum was recorded in intervals of 2 hours for a total measurement time of 42 hours and analysed with respect to shifts of FWHM, centroid and net counts of the 1332.5 keV peak.

The results can be seen in fig. 4.5(a) to 4.5(c). Here, the grey area shows the 1σ variation around the mean value. For stable operation, one would assume that these values have a Gaussian distribution around the mean value and thus about 68% of the measurement points should be inside the 1σ zone. All three measurement series satisfy this Gaussian prediction very well and the setup can be assumed to have long term stable operation condition.

4.3 Experiment at PSI

It was intended to do a first test measurement with a proton beam to check for the necessity of additional neutron or proton discrimination and get an idea of the trustworthiness of the simulations. Such a test was done at the πM1 beam line of the Paul Scherrer Institute (PSI), a designated pion beam line that can also deliver protons, and was conducted in about 8 hours of parasite beamtime granted by a befriended experiment. Due to these

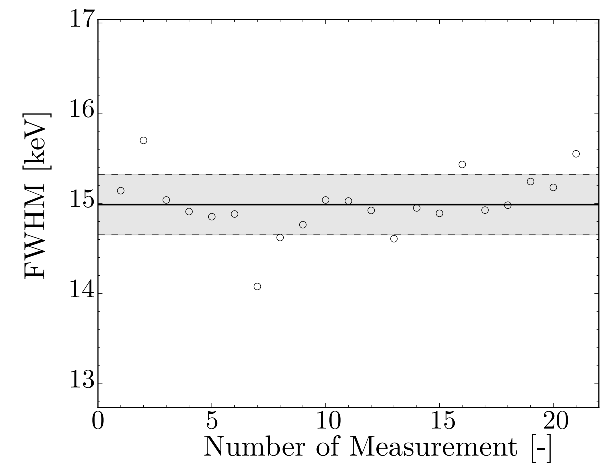

(a) FWHM

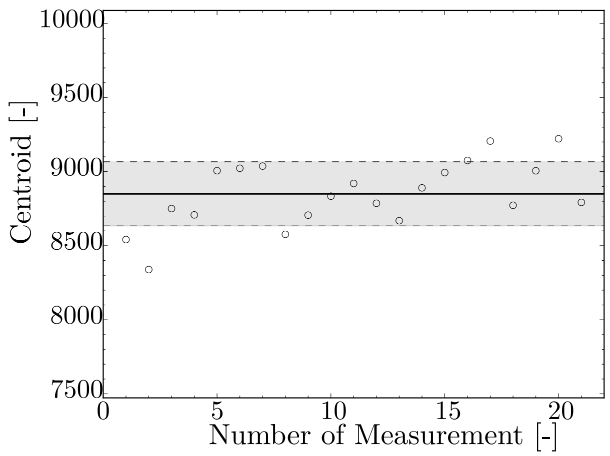

(b) Centroid

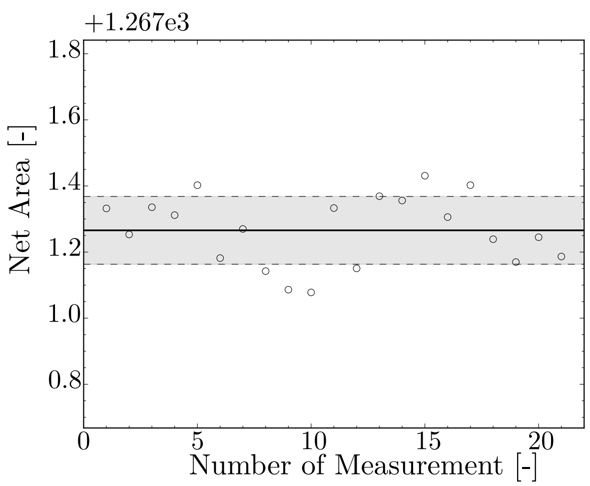

(c) Net Area

Figure 4.5: Stability measurements of the ^{60}Co spectrum with mean value and one sigma error. The variations in FWHM, centroid and net count rate fits the Gaussian prediction very well. Each spectrum was recorded for 2 hours.

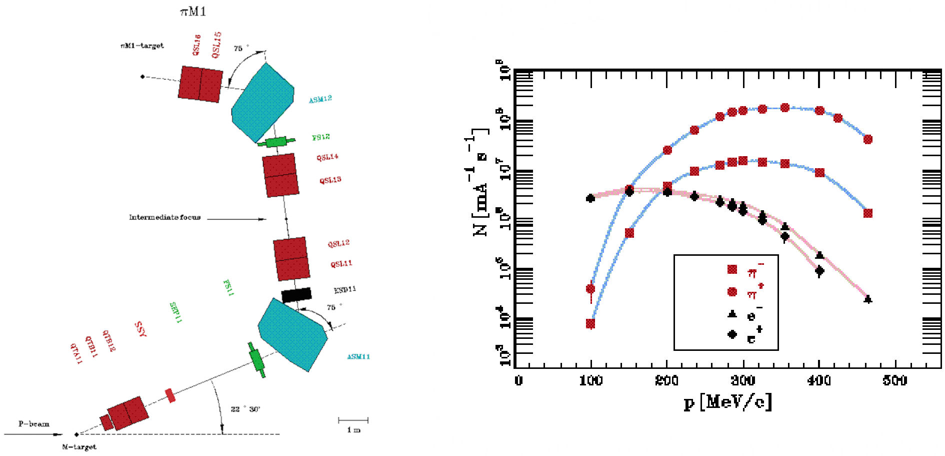

Figure 4.6: Layout of the πM1 beamline and measurement of the π^-, π^+, μ^- and μ^+ fluxes. Both graphics are taken from the PSI webpage [35]. Unfortunately, they are not available at a higher resolution.

circumstances, the measurement conditions were less than ideal in multiple aspects. Nevertheless, the data allowed for a first test of the setup and indicated its shortcomings and optimisation potential.

4.3.1 Beamline Setup

The beam delivery at the πM1 beam line starts with a 590 MeV proton beam from the large cyclotron at PSI that is shot into a graphite target. From there, a secondary beam of various particle species and deflected primary protons is extracted at an angle of 22 degree (optimised for pions) and delivered to the beam area. Unfortunately, the beam line has no electrostatic bender and is relying solely on magnetic momentum separation. For the given experimental setup it was therefore not possible to distinguish between primary p^+ and π^+. The complete layout of the beam line is shown in fig. 4.6(a) and the pion yields are given in fig. 4.6(b).

The final selection magnet was set to the highest possible value to filter for momenta of 450 MeV/c corresponding to 102.3 MeV protons (rest mass 938.3 MeV/c^2) and 331.6 MeV pions (rest mass 139.6 MeV/c^2). At these values the primary proton rate is $2 \cdot 10^6$ Hz (information from the operator) and the primary pion rate is $8 \cdot 10^7$ Hz (see fig. 4.6(b), beam current stable at approximately 2 mA). Due to radiation safety measures, the final beam blocker could not be opened to its maximum value of 500 steps (arbitrary units) but only to 100 steps, effectively cutting off large portions of the beam. The operator estimated the beam loss to be 75% of the primary beam, resulting in effective primary rates of $5 \cdot 10^5$ Hz protons and $2 \cdot 10^7$ Hz pions. Unfortunately, there was no opportunity to measure these rates and the data analysis has to rely on the estimation from the operator.

The water target had to be placed about 40 cm from the exit window of the beam line. The designed focus point of the beam line is approximately 150 cm from the exit window, which was than scaled to be at about 10 cm into the target or 50 cm from the exit window. This arrangement was necessary because the equipment of another experiment was situated at the original focus point. The short distance to the exit window of the beam has the disadvantage that deflected and then scattered particles from the beamline are more likely to reach the target or even the detector itself because the covered solid angle is increased.

The detector was placed 60 cm away from the target centre. The longitudinal position and collimator opening was varied for the different spectra. The 102.3 MeV proton beam has a CSDA range of 8.036 cm in water (NIST database [24]). Therefore, the first detector position was chosen to be placed at 8 cm and the second one at 19 cm. The lower threshold of the discriminator was set to 50 keV.

4.3.2 Results

A total of five main spectra were recorded at two different depth positions, 8 cm and 19 cm along the target, with three and two different collimator openings respectively. Four of these spectra were recorded for one hour each. The last one (19 cm depth, 0 mm opening) was recorded in only 10 minutes and therefore suffers from low statistics. In addition, a multitude of background spectra were recorded at different settings and varying durations.

The five recorded spectra and one exemplary background spectrum can be seen in fig. 4.7(a) to 4.7(f). All count rates were normalised to one second and one centimetre circumference coverage by the detector. The normalisation considering the detector coverage was done to compare the experiment, which used a single detector of 6 cm diameter, to the simulation, which used a full ring detector of 2πr circumference. For this purpose, the curvature of the detector surface was ignored. The spectra are discussed in the following section.

The background spectrum in 4.7(a) was recorded with the final beam stopper (completely) closed and the setup unchanged from the other five spectra. Another background spectrum, recorded with the final beam stopper (completely) open, no water target and a 80 MeV/c negatively charged beam going by, showed no significant difference. Unfortunately there was no spectrum recorded with the final beam stopper open to 100 steps, no water target and a 450 MeV/c beam with positive charge going by.[3] Such a measurement would have allowed inside into possible scattering from pions, that are cut off by the beam stopper, into the detector.[4]

4.3.3 Interpretation

From a first look on fig. 4.7(b) to 4.7(f) one might be irritated because they hardly differ at all. However, considering the complete setup, this is not unexpected. A summary of the integrated counts compared to simulation is given in tab. 4.2. For this comparison the counts were normalised to one primary particle. The mechanics of the simulation

[3]Such a measurement would have damaged the befriended experiment's setup.

[4]The dose deposition of 331.6 MeV positive pions after penetrating 20 cm of lead has dropped to about 50% and the drop in number of particles is significantly less. Thus it is a very real possibility that scattered and cut-off pions were penetrating beam stopper and collimator and create a direct energy deposition in the detector.

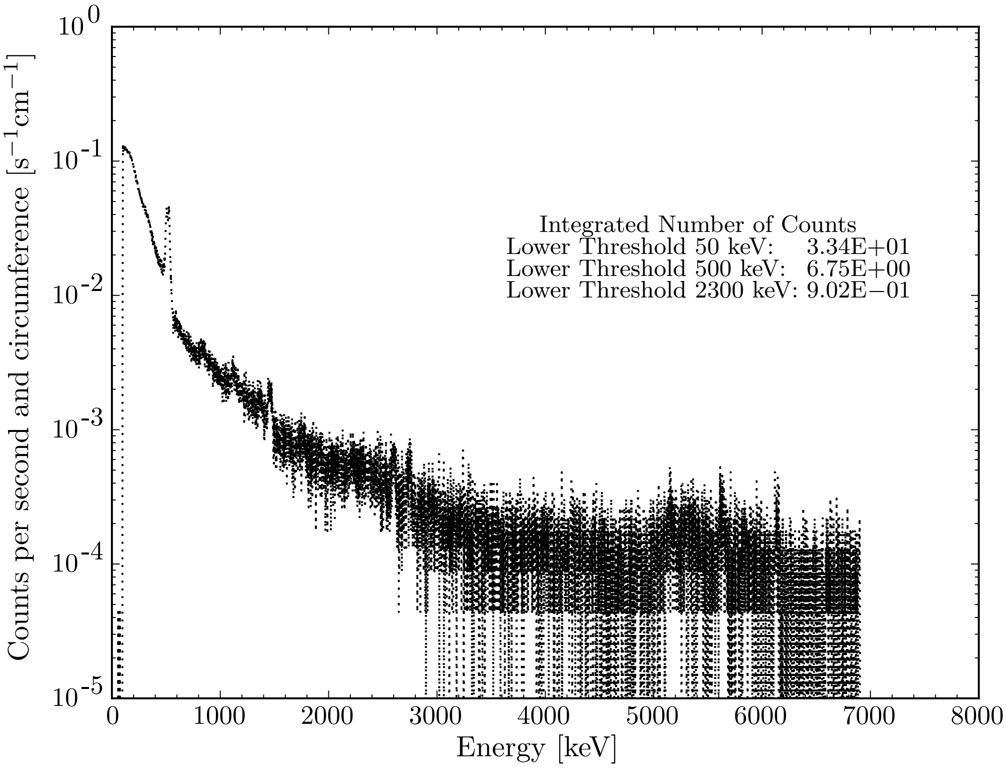

(a) Background spectrum with beam off

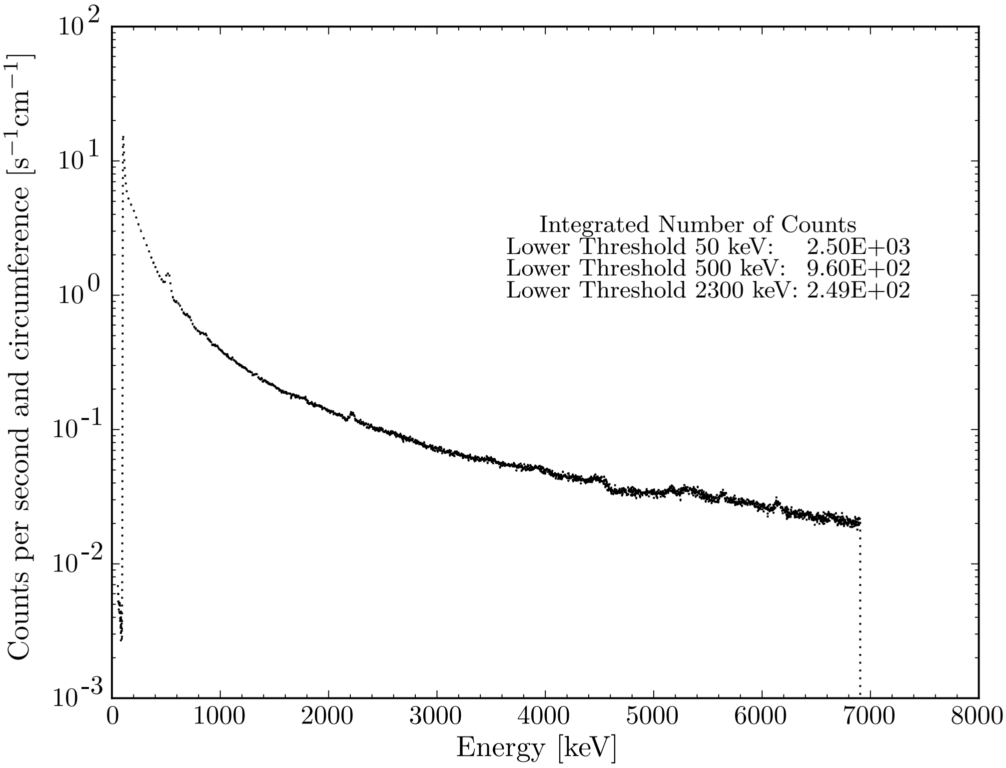

(b) position 8 cm, opening 10 mm

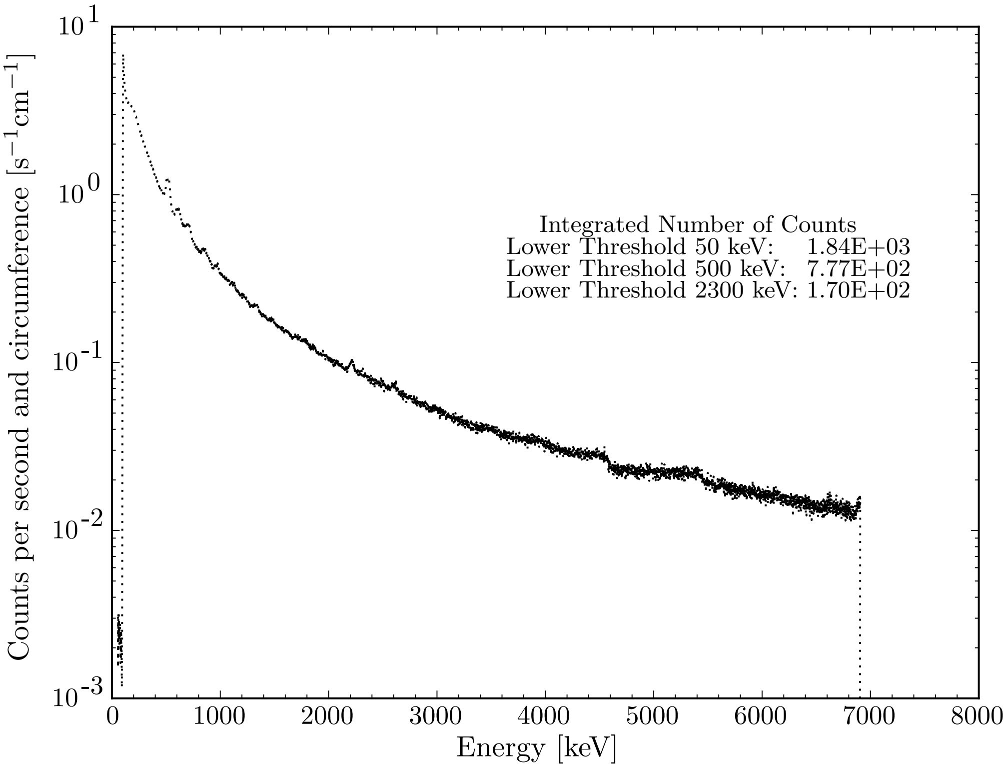

(c) position 8 cm, opening 4 mm

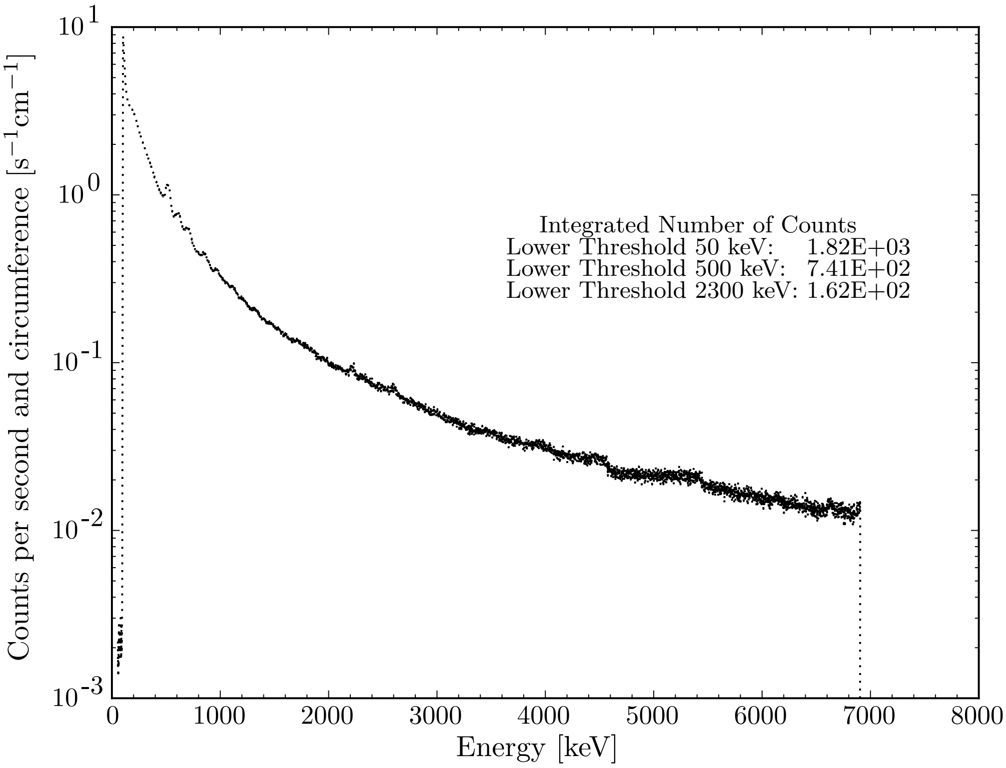

(d) position 8 cm, opening 0 mm

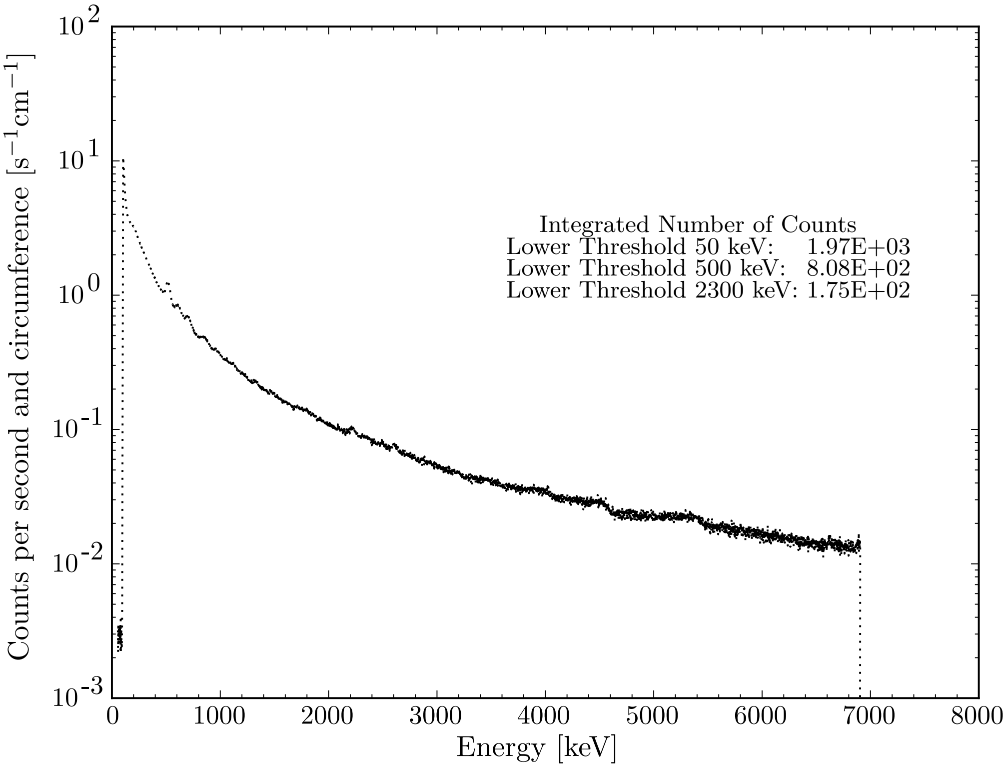

(e) position 19 cm, opening 4 mm

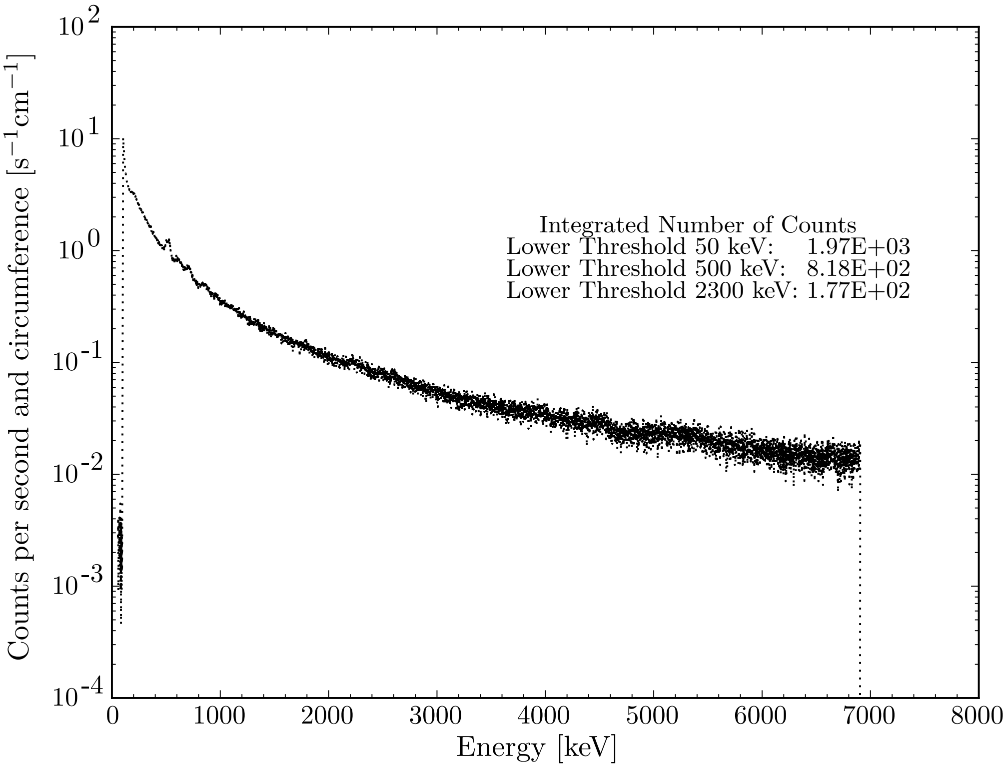

(f) position 19 cm, opening 0 mm

Figure 4.7: Background corrected spectra at different detector positions and collimator openings recorded at PSI. Normalisation to one second and one centimetre circumference coverage. Detector diameter was 5.9 cm and actual rates in the order of 10 kHz.

Table 4.2: Integrated count rates per primary particle and circumference for a lower threshold of 50 keV. The numbers from the simulation are a weighted mean of 0.024 protons and 0.976 pions.

Position	Opening	Simulation	Experiment	Deviation
8 cm	10 mm	$(4.2 \pm 0.3) \cdot 10^{-5}$	$(12.210 \pm 0.005) \cdot 10^{-5}$	(66 ± 3) %
8 cm	4 mm	$(3.9 \pm 0.3) \cdot 10^{-5}$	$(8.980 \pm 0.004) \cdot 10^{-5}$	(57 ± 3) %
8 cm	0 mm	$(3.7 \pm 0.2) \cdot 10^{-5}$	$(8.884 \pm 0.004) \cdot 10^{-5}$	(58 ± 3) %
19 cm	10 mm	$(4.6 \pm 0.3) \cdot 10^{-5}$	-	-
19 cm	4 mm	$(2.1 \pm 0.2) \cdot 10^{-5}$	$(9.618 \pm 0.004) \cdot 10^{-5}$	(79 ± 3) %
19 cm	0 mm	$(4.1 \pm 0.3) \cdot 10^{-3}$	$(9.623 \pm 0.004) \cdot 10^{-5}$	(58 ± 3) %

were the same as in section 3.3.1. Together with the recorded spectra, one makes several observations:

1. The numbers from the simulation roughly reproduce those from the experiment but are generally underestimated by a factor of 2 to 3 for most settings.
2. All five spectra look pretty similar, i.e. the structure does not change much with position or even collimation of the detector and gamma lines are barely visible.
3. The opening of the collimator has only very little effect on the count rate.
4. There is a higher count rate at 19 cm than at 8 cm.
5. In the experiment, but much more so in the simulation, there are more counts at 19 cm with 0 mm opening than with 4 mm opening. The simulation predicts that at 19 cm and 10 mm opening the count rate goes up again.
6. Overall, there is a very high count rate independent of position of the detector or opening of the collimator.

Point (1) does not really raise any concerns. First, as described in chapter 3, the choice of the physics model for hadronic processes is a very delicate matter and an agreement of about 50 % should already be considered as a good result (see [34] for one of the many reports on the accuracy of hadronic models). Secondly, the primary rate in the experiment was estimated by the operator and could easily be underestimated by a factor of 2 or 3 which would reduce the values from the experiment but has no effect on values from the simulation.

Before discussing the other five points, it is helpful to have a look at what causes the events in the detector. This is possible due to the tool of the *kill actor*. A kill actor is attached to a volume and simply removes every particle that enters this volume from the simulation. Like any other actor, it can be equipped with filters to only kill particles of a specific kind, e.g. neutrons. Any other kind of particle is unaffected by the actor and traverses the volume as it would normally do. Here, the kill actor was always attached to a very thin volume of air around the detector or target to eliminate certain particles from the simulation and see the effect on the count rate. Three sets of such simulations were conducted. From them, conclusions about the event distribution in the detector

Table 4.3: Estimation of the event distribution at the various experimental settings with a lower threshold of 50 keV. The values are based on the results from multiple simulations.

Setting	Protons	Pions
8 04	$\sim$ 68 % direct neutron $\sim$ 18 % indirect neutron - $\sim$ 14 % gamma	$\sim$ 72 % direct neutron $\sim$ 19 % indirect neutron $\sim$ 7 % pion $\sim$ 2 % gamma
8 00	$\sim$ 73 % direct neutron $\sim$ 22 % indirect neutron - $\sim$ 5 % gamma	$\sim$ 73 % direct neutron $\sim$ 19 % indirect neutron $\sim$ 7 % pion $\sim$ 1 % gamma
19 04	$\sim$ 72 % direct neutron $\sim$ 20 % indirect neutron - $\sim$ 8 % gamma	$\sim$ 44 % direct neutron $\sim$ 29 % indirect neutron $\sim$ 24 % pion $\sim$ 3 % gamma
19 00	$\sim$ 71 % direct neutron $\sim$ 21 % indirect neutron - $\sim$ 8 % gamma	$\sim$ 73 % direct neutron $\sim$ 15 % indirect neutron $\sim$ 11 % pion $\sim$ 1 % gamma

were drawn and are displayed in tab. 4.3. A table with the complete results from these simulations can be found in appendix B.

The counts that can be contributed to a direct interaction of neutrons inside the detector volume can be identified by attaching a neutron kill actor around the detector surface. This way, no neutron can enter the detector volume but neutron induced effects such as (n,γ) reactions in the collimator and shielding are still taken into account. These events can be eliminated by adding a neutron kill actor around the target itself, so that all neutrons are eliminated as soon as they leave the target. However, (n,γ) reactions inside the target are not eliminated this way and are counted as gamma events in tab. 4.3. For a primary pion beam it is also reasonable to assume that many primary pions are scattered into the detector due to their large attenuation length in water as well as lead. Therefore, these events are removed by adding a pion kill actor around the target. The number of protons reaching the detector was also measured but is negligible. The percentage value for one kind of events is then the drop in the integrated count rate when these events are removed from the simulation. At PSI, the primary beam consisted of over 97% pions and thus the effective numbers can be assumed more or less equal to the pion numbers. With this knowledge, the observations from point (2) to (6) become much clearer.

From tab. 4.3 one can see that the great majority of events in all settings are either caused by pions, neutrons or effects of neutrons in the detector surroundings. Gamma radiation from the target only contributes a few percent to the total count rate. Therefore, the gamma lines are sitting on a huge continuous background that is far less dependent on position and collimation than the gamma lines. Additionally, the low energy resolution of the detector will wash-out many gamma lines from short-lived excitation levels and such that are only weakly distinct anyway. Another point is that the production profile of gamma radiation created by pions does not show a significant drop at 8 cm like gamma radiation created by protons. Therefore, point (2) and point (6), i.e. an overall high count rate and a shape that does not change much with position and collimation, are expected for a primary beam that consists mainly of pions. Point (3) can also be contributed to the high background since the opening of the collimator has only significant influence on the gamma radiation and far less on pions and neutrons. The overall higher count rate at 19 cm than at 8 cm, that is named in point (4), is also expected when most events are created by secondary massive particles because their angular distribution is highly forward directed and they can penetrate the collimation from the side. The effect described in point (5) can not really be explained but is thought to be connected to the specific scattering angle of neutrons in the collimator gap of 4 mm. This is also supported by the fact, that the effect is gone when direct neutron events are removed from the simulation.

What to Take from the Experiment

Due to the lack of a pure proton beam, it was not possible to make a statement about the potential of prompt gamma imaging for range verification. However, it was possible to do a first test of the setup in a realistic environment and get information on its shortcomings and upgrade potential. The simulation environment could reproduce the results to a good degree and was of great assistance at interpreting the data. The experiment also showed the need to deal with the huge neutron background and that a good energy resolution might be expendable in favour of a better time resolution.

4.4 Improvements of the Setup

From the previous section it can be seen that a way of event identification is going to be indispensable for future experiments. While most of the problems that occurred at PSI could be solved by taking advantage of a dedicated proton beamline, neutron discrimination is going to be necessary nonetheless. Also, for carbon measurements discrimination of charged particles will be advantageous.

4.4.1 Discrimination of Neutrons

The discrimination of neutrons could be done in various ways. The most obvious way is to eliminate the 2.225 MeV neutron capture line from the evaluation. However, the last section showed that those events make up only a tiny fraction of the neutron events. Another option would be pulse shape analysis (PSD). However, this would not take care of neutron induced gamma creation, e.g. (n,γ) reactions in the lead collimator. A much better option is to use a fast timing detector and an event selection based on time of flight (TOF).

From fig. 4.8 one can see that the arrival of neutrons in the detector will be delayed compared to photons and thus an upper threshold of a few nanoseconds time of flight will eliminate most, if not all, direct neutron events. Additionally, this method will take care of gamma events coming from neutron capture reactions since they have relevant

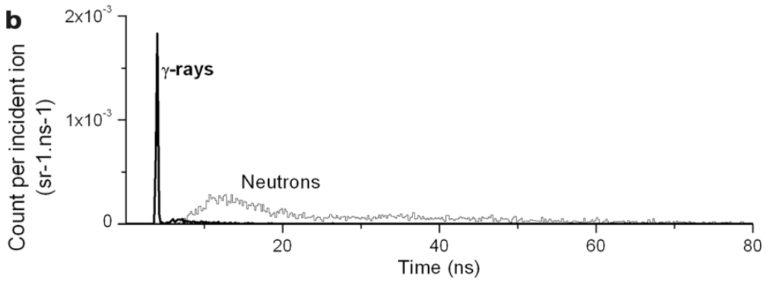

Figure 4.8: Geant4 simulated time distribution of the energy deposited in a detector positioned at 60 cm from the target with a collimator slit of 2 mm. Gamma radiation and neutrons are produced by nuclear fragmentation of 73 MeV/u carbon ions on a PMMA target. Taken from Testa et al. Nucl. Instr. and Meth. B 267 (2009) 993.

cross sections only at the end of the neutron flight path. The drawback of this approach however, is the additional material needed for a start counter which will degrade the beam quality. Also, a much faster primary detector than the HPGe is going to be necessary. For future experiments it is planned to use a BaF_2 detector of approximately the same dimensions as the HPGe detector.

Effect of Neutron Discrimination

In order to the see the effect such a TOF discrimination would have on longitudinal measurements as the ones conducted at PSI, a complete scan along the beam axis was simulated. The setup was the same as in the PSI experiments with a 102.3 MeV proton beam but the distance between detector and beam axis was reduced to 40 cm (as originally planned for PSI). The simulation was then conducted at 14 longitudinal detector positions along the target, once with a collimator opening of 4 mm and once with 0 mm. Afterwards, the whole procedure was repeated but this time a kill actor with neutron filter was attached to the target's surface. Hence, this second set of simulations eliminates all effects that are caused by neutrons outside of the target, i.e. all direct neutron events and (n,γ) events from the collimator. In contrast to a TOF selection, gamma events from neutron capture inside the target are not eliminated this way.

The results of both simulations are displayed in fig. 4.9 and 4.10. The data points in fig. 4.9 are the differences in count rate between collimator opened to 4 mm and collimator closed. Herein, 4.9(a) shows the results from the normal simulation and 4.9(b) the results after adding a neutron kill actor around the target. In both settings one can see the drop in counts at about 8 cm but the drop is more distinct with neutron discrimination. The larger errors in the simulation without neutron filter are due to the offset that is created by the neutron induced events. The need for two measurements, one with collimator closed and one with collimator opened, is problematic because any clinical application will not allow two consequent measurements. Fig. 4.10 shows the data coming only from the simulations with a 4 mm collimator opening. Without the neutron discrimination (fig. 4.10(a)) the dominating trend is a monotonic increase in depth with a weak drop around 8 cm. However, if one now adds a neutron kill actor around the target (fig. 4.10(b)), the dominating trend is mostly gone and the gamma profile emerges. The remaining increase at large depth long after the ion range can most likely be contributed to photons coming from forward scattered neutrons inside the target and should also be eliminated by a real TOF selection.

The drop is still not as distinct as the production simulations would suggest. While this has many reasons, one of them is the limited spatial resolution caused by the finite opening of the collimator. Assuming the given geometry, a perfect collimator and a production only along the target centre, the resolution as a function of the collimator opening g is

$$s(t) = g \cdot \left(1 + \frac{2}{\frac{r}{r-t} - 1}\right) \tag{4.1}$$

with detector face to target centre distance r and collimator thickness t. For values of $g = 4$ mm and $t = 20$ cm, the resolution becomes $s = 3g = 12$ mm for $r = 40$ cm (simulated setup) and $s = 5g = 20$ mm for $r = 60$ cm (setup at PSI). Considering this and the values from fig. 4.9 and 4.10, the choice of 8 cm as one of the two reference position at PSI was not perfect, not even if a pure proton beam would have been available.

4.4.2 Discrimination of Charged Particles

The discrimination of charged particles can be done by placing a thin sheet of scintillating material directly in front of the BaF_2 detector. The interaction probability for gamma radiation will be very small while for charged particles it is 100 percent and thus allows for anti-coincidence measurements.

4.4.3 Construction of the Start Counter

The start counter ultimately limits the primary rate. Therefore, it was segmented and 16 bars of 4 x 4 x 40 mm were cut from a large plate of the synthetic material BC-408. Each of them was glued on a SiPM using a optical glue. The SiPMs and the bottommost part of each scintillator were covered with latex and stored overnight to dry. Then, each individual bar was wrapped in thin aluminium foil[5] to obtain a maximum reflection of the scintillation light. Afterwards, eight bars each were packed together and wrapped into black tape. The border regions between tape and aluminium as well as the remaining surface regions were again covered in latex to make sure that no light from the outside can reach the scintillating bar. Both packs were put into a 3D printed frame, one layer oriented in x direction and one in y direction. The schematics of the start counter can be seen in fig. 4.11 and some pictures from the construction process in fig. 4.12.

4.4.4 Testing of the Start Counter

A first test with the start counter was done by measuring coincidences between the two layers. Therefore, an improvised collimator consisting of two pieces of metal approximately one and a half centimetre thick was put above the start counter and on top of it a ^{90}Sr

[5]This sequence of action was important to make sure that the aluminium can not touch the open pins of the SiPM.

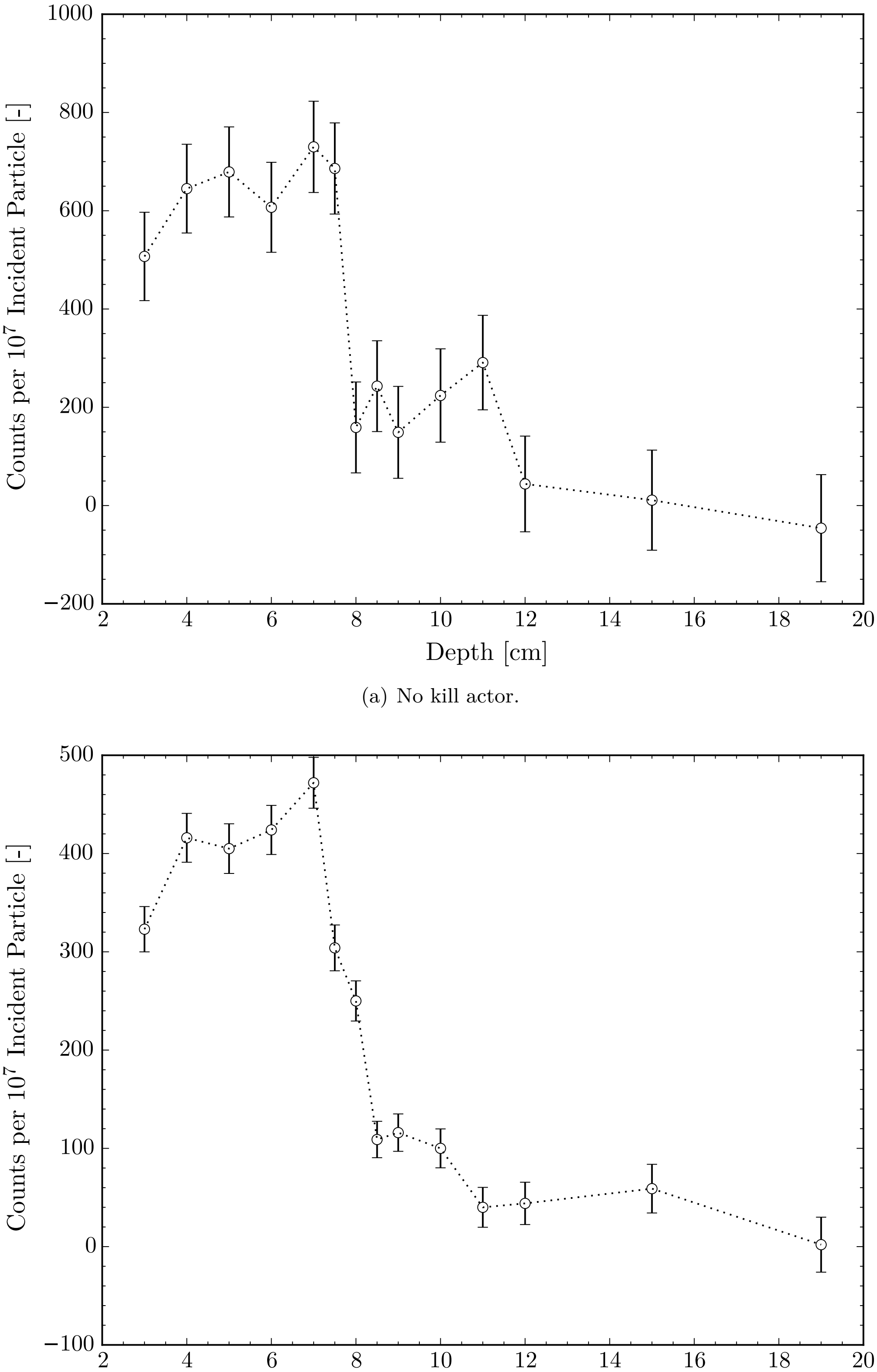

Figure 4.9: Longitudinal scan of the difference in count rates between 4 mm and 0 mm collimator opening. Incident particles are 102.3 MeV protons. Simulation in GATE.

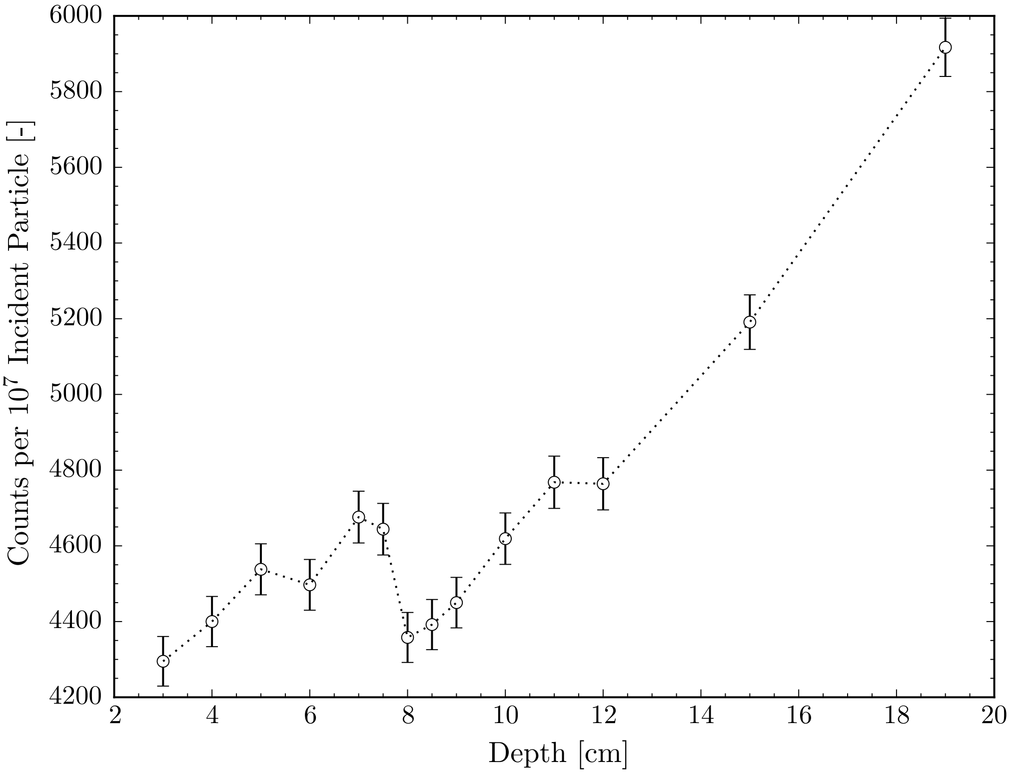

(a) No kill actor.

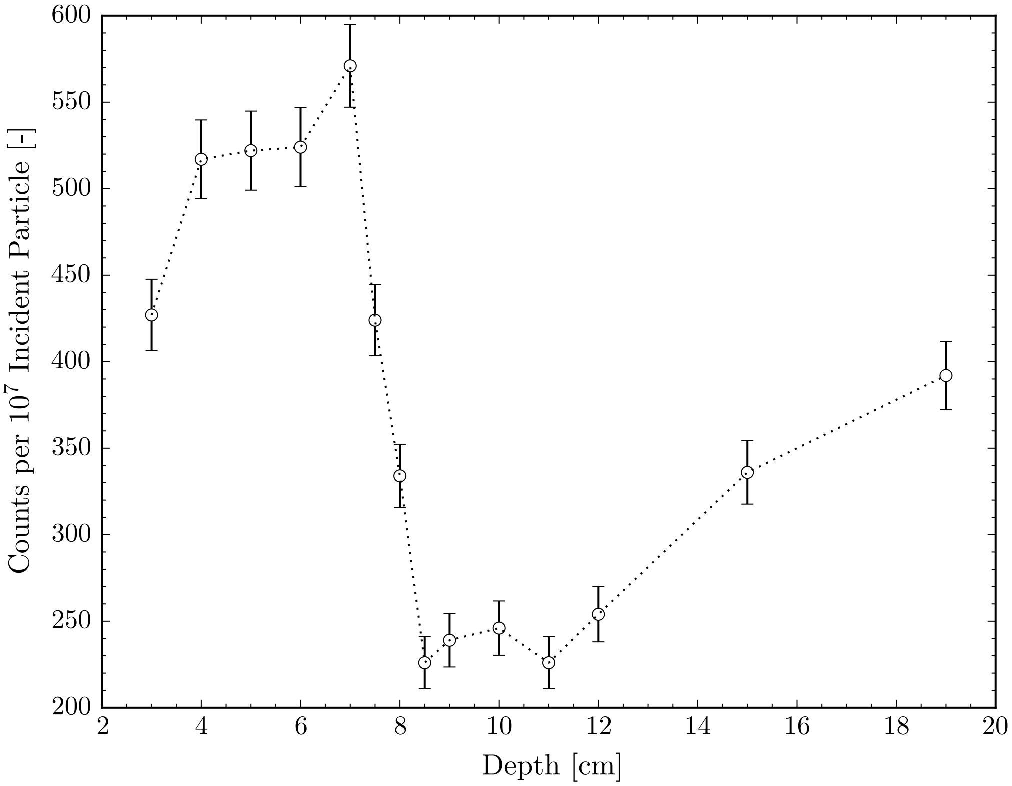

(b) Neutron kill actor around the target.

Figure 4.10: Longitudinal scan with 4 mm opening. Incident particles are 102.3 MeV protons. Simulation in GATE.

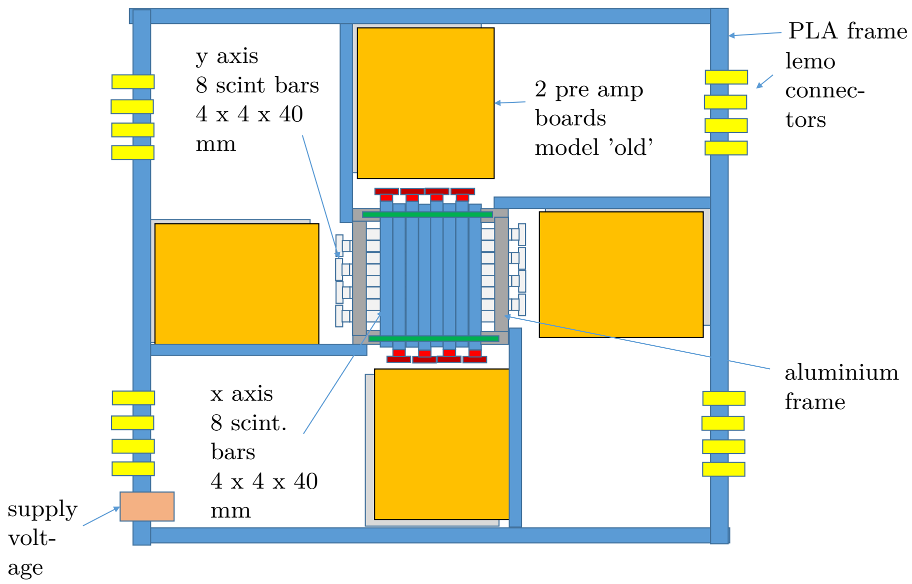

Figure 4.11: Schematics of the start counter.

source. The main emission products of this source are 0.546 MeV and 2.284 MeV electrons. With this setup, the possible interaction region for coincidences is restricted to the two cubes of 4 × 4 × 4 mm at top of each other. A simple electrical circuit as displayed in fig. 4.13(a) was build to trigger only on coincident events. The events were then recorded on an oscilloscope with a 40 GHz/s sampling rate.

To allow a test of the time of flight capabilities of the start counter under normal laboratory conditions (i.e. no high energetic proton beam is available), the TOF measurement was done between the two layers of the counter, without a gap between them to improve efficiency. Since the two layers are so close to each other, one can not hope to resolve the timing difference $\Delta t = t_2 - t_1$. In fact, for a coincidence interaction region 10 mm from the SiPM's, the jitter resulting from the uncertainty of the interaction point is already of the order of the time difference that results from the 4 mm centre to centre separation of the two bars. Additionally, there is the uncertainty of scintillation light scattering inside the bars, lifetime of the excited states, jitter coming from the SiPM and also the time resolution of the oscilloscope. One possible test however, is to create an asymmetry on purpose and see if the measurement can reproduce it.

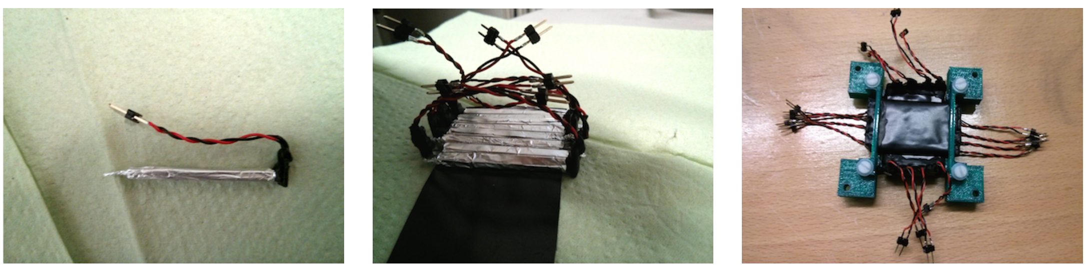

Figure 4.12: Construction of the start counter/beam profiler.

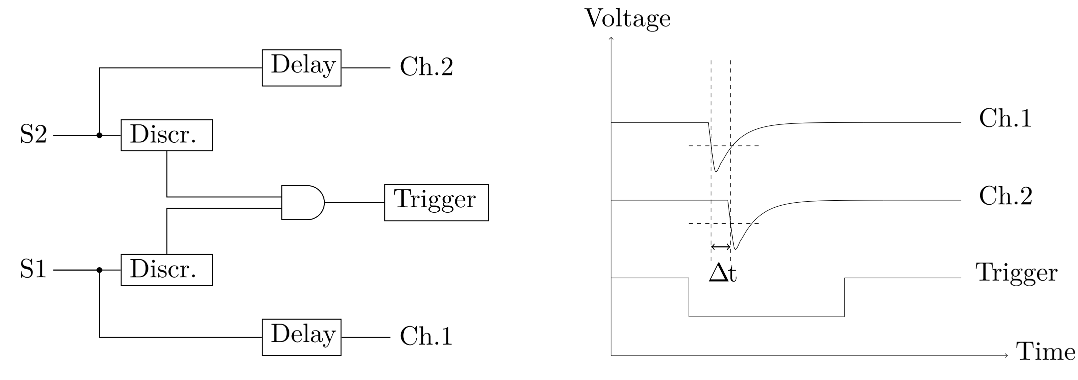

(a) The DAQ circuit. (b) A typical signal.

Figure 4.13: The coincidence measurement setup.

Let ξ be the ratio of the number of events that show $\Delta t > 0$ to the total number of events, i.e.

$$\xi = \frac{N_{\Delta t>0}}{N_{tot}} \tag{4.2}$$

The minimum travel distance s_i for direct photons can be assumed as the distance between the centre of the interaction region and the SiPM. For a symmetric travel path, i.e. $s_1 \approx s_2$, one can assume that the jitter will dominate and on average we will have $\xi \approx 0.5$. However, if one chooses asymmetric travel paths, i.e. $s_2 > s_1$, the ratio should shift in favour of the shorter travel path.

Two measurements, one with $s_2 \approx s_1 \approx 10$ mm and one with $s_2 \approx 3s_1 \approx 30$ mm, were conducted with about 200 coincidence events each. The timing difference was calculated by constant fraction discrimination at 20%. The results can be seen in tab. 4.4. While the timing measurements themselves show a very large uncertainty as expected (even when choosing only 'valid' events with $\Delta t > 0$), the ratio ξ shifts from 0.48 to 0.74 due to the longer travel path in the lower layer. Therefore, this result provides evidence that the setup is working correctly.

	Measurement 1	Measurement 2
$s_x : s_y$	1:1	3:1
Δt_{tot}	(310 ± 1550) ps	(280 ± 240) ps
Δt_{pos}	(220 ± 240) ps	(290 ± 240) ps
ξ	0.48	0.74

Table 4.4: Results from the coincidence measurements. Each result was sampled from about 200 events. The quantity Δt_{pos} indicates the timing result when ignoring all 'non valid' events, i.e. such where $\Delta t < 0$.

Chapter 5

Outlook

In this work, the possibility to use prompt gamma radiation to determine the ion range in ion therapy has been investigated. A versatile detector setup was built and tested at PSI. The recorded data could be reproduced by the simulation environment GATE. Apart from the technical preparations for future measurements, the main result of this thesis is the necessity of particle identification to reduce the neutron background. Ideally, this is done with fast timing detectors.

Certainly, imaging in ion therapy will play an essential role in improving radiation treatment quality. The three main approaches at this point are PGI (Prompt Gamma Imaging), IVI (Interaction Vertex Imaging) and PET (Positron Emission Tomography), which were discussed in section 1.2. In the first stage of clinical application, each of them will most likely be used to calibrate the ion range prior to the actual dose delivery. With increasing experience and improved prototypes it should then be possible to map the delivered dose distribution during the treatment. It is important to point out that the three approaches do not exclude each other and could be used at the same time, providing that a suitable detector system is available. Indeed, the combination of two or even three independent measurements would increase the accuracy and reduce the systematic error of event reconstruction. There are already several approaches going in this direction. The INSIDE project (Innovative Solutions for In-beam Dosimetry in Hadrontherapy) aims to combine in-beam PET with IVI [36]. The AQUA program [37] (Advanced Quality Assurance) goes another step further and plans to build a complete multi-purpose detector system that would allow to combine in-beam PET with IVI and two forms of proton tomography (Nuclear Scattering Tomography and Proton Range Radiography). Besides the combination of different methods, it will be important to find new detector solutions for the individual applications and gain a better understanding of the correlation between the deposited dose and the ion-induced activity. A systematic study of the production cross sections for prompt gammas, prompt protons and beta plus emitters over a large energy region and for all relevant elements will certainly help with the latter and increase the quality of simulations.

Appendix A

GATE

GATE, the *Geant4 Application for Emission Tomography*, is a simple macro language that builds around Geant4 and uses it to generate particles and simulate their transport through different materials. It is developed by the OpenGate Collaboration. From their wiki page: "GATE (...) encapsulates the Geant4 libraries in order to achieve a modular, versatile, scripted simulation toolkit adapted to the field of nuclear medicine."

GATE simulations are written in .mac files and then executed with

```
Gate example.mac
```

The following is a short example of a GATE macro file to measure the dose and gamma production along the z axis as described in chapter 2.

```
# ======================================================
# PREPERATIONS
# ======================================================

# Set engine
/gate/random/setEngineSeed auto

# Set material database, must be provided externally
/gate/geometry/setMaterialDatabase GateMaterials.db

# Create world
/gate/world/geometry/setXLength 1. m
/gate/world/geometry/setYLength 1. m
/gate/world/geometry/setZLength 1. m
/gate/world/setMaterial Air
/gate/world/vis/forceWireframe
/gate/world/describe

# Set up statistics actor
/gate/actor/addActor SimulationStatisticActor stats
/gate/actor/stats/save output/statistics.txt

# Load physics list, must be provided externally
/control/execute physics.mac

```

```

# ======================================================
# TARGET
# ======================================================

# Set up the volume
/gate/world/daughters/name phantom
/gate/world/daughters/insert cylinder
/gate/phantom/setMaterial Water
/gate/phantom/vis/setColor blue
/gate/phantom/vis/forceWireframe
/gate/phantom/geometry/setRmax 10. cm
/gate/phantom/geometry/setRmin 0. cm
/gate/phantom/geometry/setHeight 50. cm
/gate/phantom/placement/setTranslation 0. 0. 0. cm

# Set up dose actor
/gate/actor/addActor DoseActor dose
/gate/actor/dose/attachTo phantom
/gate/actor/dose/save output/dose.txt
/gate/actor/dose/stepHitType random
/gate/actor/dose/setResolution 1 1 500
/gate/actor/dose/enableDose true

# Set up production actor with gamma filter
/gate/actor/addActor ProductionAndStoppingActor gamma_prod
/gate/actor/gamma_prod/save output/gamma_prod.txt
/gate/actor/gamma_prod/attachTo phantom
/gate/actor/gamma_prod/setResolution 1 1 500
/gate/actor/gamma_prod/stepHitType post
/gate/actor/gamma_prod/addFilter particleFilter
/gate/actor/gamma_prod/particleFilter/addParticle gamma


# ======================================================
# VISUALISATION
# ======================================================

# Set up the viewer
/vis/open OGLIX
/vis/viewer/reset
/vis/viewer/zoom 2.0
/vis/viewer/set/viewpointThetaPhi 60 70
/vis/viewer/set/style surface
/vis/drawVolume
/tracking/storeTrajectory 1
/vis/scene/add/trajectories
/vis/scene/endOfEventAction accumulate 10
/vis/viewer/update

# Update the view
/vis/viewer/refresh

# Initialise the setup
/gate/run/initialize
```

```


# =====================================================
# SOURCE
# =====================================================

# Create gaussian proton beam of 100 MeV
/gate/source/addSource H1 gps
/gate/source/H1/gps/particle proton
/gate/source/H1/gps/energytype Mono
/gate/source/H1/gps/monoenergy 100. MeV
/gate/source/H1/gps/pos/type Beam
/gate/source/H1/gps/pos/shape Circle
/gate/source/H1/gps/pos/centre 0.0 0.0 40.0 cm
/gate/source/H1/gps/direction 0 0 1

# Set sigma and emittance of the beam
/gate/source/H1/gps/pos/sigma_x 3.0 mm
/gate/source/H1/gps/pos/sigma_y 3.0 mm
/gate/source/H1/gps/ang/type beam2d
/gate/source/H1/gps/ang/sigma_x 0 deg
/gate/source/H1/gps/ang/sigma_y 0 deg

# Display source info
/gate/source/list


# =====================================================
# EXECUTION
# =====================================================

# Disable visualisation and start simulation for 100 primaries
/vis/disable
/gate/application/setTotalNumberOfPrimaries 100
/gate/application/start
```

Appendix B

Raw Data from Simulations

The raw data from the information displayed in tab. 4.3 can be seen in the following tables. The legend is the following: 'sim' stands for the normal simulation with any kill actor, 'filter n det' is for the simulation with a kill actor around the detector to eliminate direct neutron events, 'filter n target' are the numbers from the simulation with a kill actor around the target to eliminate all neutron induced events outside the target and 'filter n pi p target' are those for a neutron, pion and proton kill actor around the target. The counts above 50 keV per incident particle from a primary proton beam of 102.3 MeV are

Position	Opening	Sim	Filter n det	Filter n target
08	00	$6.0 \cdot 10^{-7}$	$1.7 \cdot 10^{-7}$	$2.9 \cdot 10^{-8}$
08	04	$7.2 \cdot 10^{-7}$	$2.3 \cdot 10^{-7}$	$10.1 \cdot 10^{-8}$
08	10	$13.2 \cdot 10^{-7}$	$6.7 \cdot 10^{-7}$	$57.3 \cdot 10^{-8}$
19	00	$9.6 \cdot 10^{-7}$	$2.8 \cdot 10^{-7}$	$7.6 \cdot 10^{-8}$
19	04	$9.9 \cdot 10^{-7}$	$2.8 \cdot 10^{-7}$	$7.4 \cdot 10^{-8}$
19	10	$10.0 \cdot 10^{-7}$	$3.5 \cdot 10^{-7}$	$12.8 \cdot 10^{-8}$

from a primary pion beam of 331.6 MeV

Position	Opening	Sim	Filter n det	Filter n target	Filter n pi p target
08	00	$3.8 \cdot 10^{-5}$	$1.0 \cdot 10^{-5}$	$3.1 \cdot 10^{-6}$	$6.2 \cdot 10^{-7}$
08	04	$4.0 \cdot 10^{-5}$	$1.1 \cdot 10^{-5}$	$3.5 \cdot 10^{-6}$	$8.6 \cdot 10^{-7}$
08	10	$4.3 \cdot 10^{-5}$	$1.3 \cdot 10^{-5}$	$5.1 \cdot 10^{-6}$	$22.8 \cdot 10^{-7}$
19	00	$4.2 \cdot 10^{-5}$	$1.1 \cdot 10^{-5}$	$5.1 \cdot 10^{-6}$	$4.7 \cdot 10^{-7}$
19	04	$2.1 \cdot 10^{-5}$	$1.2 \cdot 10^{-5}$	$5.6 \cdot 10^{-6}$	$7.3 \cdot 10^{-7}$
19	10	$4.7 \cdot 10^{-5}$	$1.4 \cdot 10^{-5}$	$7.4 \cdot 10^{-6}$	$21.2 \cdot 10^{-7}$

and the weighted mean of 0.024 protons and 0.976 pions gives

Position	Opening	Sim	Filter n det	Filter n target	Filter n pi p target
08	00	$3.7 \cdot 10^{-5}$	$1.0 \cdot 10^{-5}$	$3.0 \cdot 10^{-6}$	$6.1 \cdot 10^{-7}$
08	04	$3.9 \cdot 10^{-5}$	$1.1 \cdot 10^{-5}$	$3.4 \cdot 10^{-6}$	$8.4 \cdot 10^{-7}$
08	10	$4.2 \cdot 10^{-5}$	$1.3 \cdot 10^{-5}$	$4.9 \cdot 10^{-6}$	$22.4 \cdot 10^{-7}$
19	00	$4.1 \cdot 10^{-5}$	$1.1 \cdot 10^{-5}$	$4.9 \cdot 10^{-6}$	$4.6 \cdot 10^{-7}$
19	04	$2.0 \cdot 10^{-5}$	$1.2 \cdot 10^{-5}$	$5.5 \cdot 10^{-6}$	$7.2 \cdot 10^{-7}$
19	10	$4.6 \cdot 10^{-5}$	$1.4 \cdot 10^{-5}$	$7.2 \cdot 10^{-6}$	$21.6 \cdot 10^{-7}$

Bibliography

[1] R. R. Wilson, "Radiological use of fast protons," *Radiology*, vol. 47, pp. 487–491, 1946.

[2] D. Schardt, T. Elsässer, and D. Schulz-Ertner, "Heavy-ion tumor therapy: Physical and radiobiological benefits," *Review of Modern Physics*, vol. 82, pp. 383–425, Feb 2010.

[3] P. Preuss, "The promise of ion beam cancer therapy." `http://newscenter.lbl.gov/2010/10/18/ion-beam-therapy/`, 2010. [Online, Berkeley Lab News Center; accessed 29 December 2014].

[4] C. Kurz, A. Mairani, and K. Parodi, "First experimental-based characterization of oxygen ion beam depth dose distributions at the Heidelberg Ion-Beam Therapy Center," *Physics in Medicine and Biology*, vol. 57, p. 5017–5034, 2012.

[5] N. Bassler, J. Alsner, G. Beyer, J. DeMarco, M. Doser, D. Hajdukovic, O. Hartley, K. Iwamoto, O. Jaekel, H. V. Knudsen, S. Kovacevic, S. Møller, J. Overgaard, J. Jørgen B. Petersen, T. Solberg, B. Sørensen, K. Vranjes, B. Wouter, and M. Holzscheiter, "Antiproton radiotherapy," *Radiotherapy and Oncology*, vol. 86, pp. 14–19, 2008.

[6] H. Paganetti, "Range uncertainties in proton therapy and the role of monte carlo simulations," *Physics in Medicine and Biology*, vol. 57, no. 11, p. R99, 2012.

[7] K. Parodi, "PET monitoring of hadrontherapy," *Nuclear Medicine Review*, vol. 15, pp. C37 – C42, 2012.

[8] K. Parodi, T. Bortfeld, W. Enghardt, F. Fiedler, A. Knopf, H. Paganetti, J. Pawelke, G. Shakirin, and H. Shih, "PET imaging for treatment verification of ion therapy: Implementation and experience at GSI Darmstadt and MGH Boston," *Nuclear Instruments and Methods in Physics Research Section A*, vol. 591, no. 1, pp. 282 – 286, 2008. Radiation Imaging Detectors 2007 Proceedings of the 9th International Workshop on Radiation Imaging Detectors.

[9] W. Enghardt, P. Crespo, F. Fiedler, R. Hinz, K. Parodi, J. Pawelke, and F. Pönisch, "Charged hadron tumour therapy monitoring by means of PET," *Nuclear Instruments and Methods in Physics Research Section A*, vol. 525, no. 1–2, pp. 284 – 288, 2004. Proceedings of the International Conference on Imaging Techniques in Subatomic Physics, Astrophysics, Medicine, Biology and Industry.

[10] P. Henriquet, E. Testa, M. Chevallier, D. Dauvergne, G. Dedes, N. Freud, J. Krimmer, J. M. Létang, C. Ray, M.-H. Richard, and F. Sauli, "Interaction vertex imaging (IVI)

for carbon ion therapy monitoring: a feasibility study," *Physics in Medicine and Biology*, vol. 57, no. 14, p. 4655 – 4669, 2012.

[11] K. Gwosch, B. Hartmann, J. Jakubek, C. Granja, P. Soukup, O. Jäkel, and M. Martišíková, "Non-invasive monitoring of therapeutic carbon ion beams in a homogeneous phantom by tracking of secondary ions," *Physics in Medicine and Biology*, vol. 58, no. 11, pp. 3755 – 3773, 2013.

[12] W. Assmann, S. Kellnberger, S. Reinhardt, S. Lehrack, A. Edlich, P. G. Thirolf, M. Moser, G. Dollinger, M. Omar, V. Ntziachristos, and K. Parodi, "Ionoacoustic characterization of the proton Bragg peak with submillimeter accuracy," *Medical Physics*, vol. 42, no. 2, pp. 567–574, 2015.

[13] F. Stichelbaut and Y. Jongen. Meeting of the 39th Particle Therapy Cooperative Group, San Francisco, October 2003 (unpublished).

[14] P. Dyer, D. Bodansky, A. G. Seamster, E. B. Norman, and D. R. Maxson, "Cross sections relevant to gamma-ray astronomy: Proton induced reactions," *Physical Review C*, vol. 23, pp. 1865–1882, May 1981.

[15] C. H. Min, C. H. Kim, M. Y. Youn, and J. W. Kim, "Prompt gamma measurements for locating the dose falloff region in the proton therapy," *Applied Physics Letters*, vol. 89, p. 183517, 2006.

[16] E. Testa, M. Bajard, M. Chevallier, D. Dauvergne, F. L. Foulher, N. Freud, J. Létang, J. Poizat, C. Ray, and M. Testa, "Dose profile monitoring with carbon ions by means of prompt-gamma measurements," *Nuclear Instruments and Methods in Physics Research Section B*, vol. 267, no. 6, pp. 993 – 996, 2009. Proceedings of the Seventh International Symposium on Swift Heavy Ions in Matter.

[17] J. C. Polf, R. Panthi, D. S. Mackin, M. McCleskey, A. Saastamoinen, B. T. Roeder, and S. Beddar, "Measurement of characteristic prompt gamma rays emitted from oxygen and carbon in tissue-equivalent samples during proton beam irradiation," *Physics in Medicine and Biology*, vol. 58, no. 17, p. 5821, 2013.

[18] F. Janssen, G. Landry, P. C. Lopes, G. Dedes, J. Smeets, D. R. Schaart, K. Parodi, and F. Verhaegen, "Factors influencing the accuracy of beam range estimation in proton therapy using prompt gamma emission," *Physics in Medicine and Biology*, vol. 59, no. 15, p. 4427, 2014.

[19] C. H. Min, H. R. Lee, C. H. Kim, and S. B. Lee, "Development of array-type prompt gamma measurement system for in vivo range verification in proton therapy," *Medical Physics*, vol. 39, no. 4, pp. 2100–2107, 2012.

[20] M. Yamaguchi, "Development of head module for multi-head si/cdte compton camera for medical applications," *Nuclear Instruments and Methods in Physics Research Section A*, vol. 648, Supplement 1, no. 0, pp. S2 – S7, 2011. NIM A 4th International Conference on Imaging techniques in Subatomic Physics, Astrophysics, Medicine, Biology and Industry.

[21] J. Smeets, F. Roellinghoff, D. Prieels, F. Stichelbaut, A. Benilov, P. Busca, C. Fiorini, R. Peloso, M. Basilavecchia, T. Frizzi, J. C. Dehaes, and A. Dubus, "Prompt gamma imaging with a slit camera for real-time range control in proton therapy," *Physics in Medicine and Biology*, vol. 57, no. 11, p. 3371, 2012.

[22] U. Fano, "Penetration of Protons, Alpha Particles, and Mesons," *Annual Review of Nuclear and Particle Science*, vol. 13, pp. 1–66, 1963.

[23] R. Golser, "Fundamental aspects of ion electron interactions," in *Application of Particle and Laser Beams in Materials Technology* (P. Misaelides, ed.), vol. 283 of *NATO ASI Series*, pp. 1–20, Springer Netherlands, 1995.

[24] NIST, "PSTAR Database." `http://www.nist.gov/pml/data/star/index.cfm`, 2015. [Online, National Institute of Standards and Technology; accessed March 16, 2015].

[25] R. Serber, "Nuclear reactions at high energies," *Physical Review*, vol. 72, pp. 1114–1115, Dec 1947.

[26] R. Ramaty, B. Kozlovsky, and R. E. Lingenfelter, "Nuclear gamma-rays from energetic particle interactions," *Astrophysical Journal Supplement Series*, vol. 40, pp. 487–526, Jul 1979.

[27] F. Le Foulher, M. Bajard, M. Chevallier, D. Dauvergne, N. Freud, P. Henriquet, S. Karkar, J. Létang, L. Lestand, R. Plescak, C. Ray, D. Schardt, E. Testa, and M. Testa, "Monte Carlo simulations of prompt-gamma emission during carbon ion irradiation," *IEEE Transactions on Nuclear Science*, vol. 57 (5), pp. 2768–2772, 2010. accepted for publication in IEEE TNS.

[28] S. Jan, G. Santin, D. Strul, S. Staelens, K. Assié, D. Autret, S. Avner, R. Barbier, M. Bardiès, P. M. Bloomfield, D. Brasse, V. Breton, P. Bruyndonckx, I. Buvat, A. F. Chatziioannou, Y. Choi, Y. H. Chung, C. Comtat, D. Donnarieix, L. Ferrer, S. J. Glick, C. J. Groiselle, D. Guez, P.-F. Honore, S. Kerhoas-Cavata, A. S. Kirov, V. Kohli, M. Koole, M. Krieguer, D. J. van der Laan, F. Lamare, G. Largeron, C. Lartizien, D. Lazaro, M. C. Maas, L. Maigne, F. Mayet, F. Melot, C. Merheb, E. Pennacchio, J. Perez, U. Pietrzyk, F. R. Rannou, M. Rey, D. R. Schaart, C. R. Schmidtlein, L. Simon, T. Y. Song, J.-M. Vieira, D. Visvikis, R. V. de Walle, E. Wieërs, and C. Morel, "GATE: a simulation toolkit for PET and SPECT," *Physics in Medicine and Biology*, vol. 49, p. 4543–4561, 2004.

[29] OpenGATE Collaboration, "GATE Users Guide v6.2." `http://wiki.opengatecollaboration.org/index.php/Users_Guide_V6.2`, 2015. [Online, OpenGATE Collaboration Wiki; accessed 5 January 2015].

[30] Geant4 Collaboration, "Geant4 Reference Physics List." `http://geant4.cern.ch/support/proc_mod_catalog/physics_lists/referencePL.shtml`, 2015. [Online, Geant4 User Support; accessed 16 April 2015].

[31] Geant4 Collaboration, "Geant4 Physics Reference Manual." `http://geant4.web.cern.ch/geant4/G4UsersDocuments/UsersGuides/PhysicsReferenceManual/html/PhysicsReferenceManual.html`, 2015. [Online, Geant4 Users' Documents; accessed 16 April 2015].

[32] Brookhaven National Laboratory, "NuDat 2.6." `http://www.nndc.bnl.gov/nudat2/`, 2015. [Online, National Nuclear Data Center; accessed 28 April 2015].

[33] T. A. Prince, J. C. Ling, W. A. Mahoney, G. R. Riegler, and A. S. Jacobson, "A high-resolution measurement of the 2.223 MeV neutron capture line in a solar flare," *Astrophysical Journal, Part 2 - Letters to the Editor*, vol. 255, pp. L81–L84, 1982.

[34] J. M. Verburg, H. A. Shih, and J. Seco, "Simulation of prompt gamma-ray emission during proton radiotherapy," *Physics in Medicine and Biology*, vol. 57, no. 17, p. 5459, 2012.

[35] PSI, "piM1 area." `http://aea.web.psi.ch/beam2lines/beam_pim1.html`, 2015. [Online, Paul Scherrer Institute; accessed March 17, 2015].

[36] Vincenzo Patera, "The INSIDE project." Presentation given at the ICTR-PHE 2014 conference, Geneva, 12th February 2014.

[37] TERA Foundation, "Project AQUA." `http://project-aqua.web.cern.ch/project-aqua/`, 2015. [Online, Project AQUA website; accessed April 25, 2015].

Curriculum Vitae

Education

University of Vienna, Vienna, Austria

M.Sc., Physics, March 2013 to July 2015

- Specialisation in Experimental Nuclear and Particle Physics
- Thesis Topic: *Investigations on Prompt Gamma Imaging as Range Verification Method for Ion Therapy*
- Supervisor: Prof. Johann Zmeskal, Stefan Meyer Institute for Subatomic Physics
- Main task: Planning and constructing an experimental setup (hard- and software) to measure the longitudinal distribution of prompt gamma production in water after proton irradiation. Conducting the experiment within a beamtime at PSI, Switzerland.

B.Sc., Physics, October 2009 to March 2013

- Thesis Topic: *Ion Therapy and MedAustron*
- Supervisor: Prof. Eberhard Widmann, Stefan Meyer Institute for Subatomic Physics

BRG Feldkirchen, Feldkirchen, Austria

High School Graduation, June 2008

Schools and Training

University of Novi Sad, Novi Sad, Serbia

CERN Danube School on Instrumentation in Particle & Nuclear Physics, September 2014

Stefan Meyer Institute, Vienna, Austria

Summer Student Programme, August 2013

Service

Diakonie Waiern, Feldkirchen, Austria

Civil Service, September 2008 to Mai 2009